IEEE Access
Multidisciplinary ⋮ Rapid Review ⋮ Open Access Journal

Received 7 October 2022, accepted 20 October 2022, date of publication 26 October 2022, date of current version 3 November 2022.

Digital Object Identifier 10.1109/ACCESS.2022.3217243

RESEARCH ARTICLE

Curvature Best Basis: A Novel Criterion to Dynamically Select a Single Best Basis as the Extracted Feature for Periocular Recognition

REGINA LIONNIE[1], (Graduate Student Member, IEEE), CATUR APRIONO[1], (Member, IEEE), RIFAI CHAI[2], (Senior Member, IEEE), AND DADANG GUNAWAN[1], (Senior Member, IEEE)

[1]Department of Electrical Engineering, Universitas Indonesia, Kampus Baru UI Depok, Depok, Jawa Barat 16424, Indonesia
[2]School of Science, Computing and Engineering Technologies, Swinburne University of Technology, Hawthorn, VIC 3122, Australia

Corresponding author: Dadang Gunawan (guna@eng.ui.ac.id)

This work was supported by the Directorate of Research and Development, Universitas Indonesia under Hibah Publikasi Terindeks Internasional (PUTI) 2022 under Grant NKB-682/UN2.RST/HKP.05.00/2022.

ABSTRACT Aiming at the problems in the best basis selection, this paper presents a novel criterion based on the statistical measurement of the curvature wavelet coefficient to dynamically select the single best basis of the quad-tree wavelet packet transformation. The selected single best basis works as an extracted feature for biometric periocular recognition system. The proposed method first extracts the mean curvature of wavelet coefficients inside the quad-tree wavelet packet transform. Second, the method finds the most distinctive features based on the largest standard deviation and dynamically selects the extracted curvature wavelet coefficients as the single best basis. Third, the selected single curvature best basis works as an extracted feature, and then it is combined with the histogram of oriented gradients method. Finally, the support vector machine is employed to perform classification. Two datasets of two-dimensional periocular digital images are tested against the proposed method. To show the extended ability, we analyze the curvature best basis method against wavelet functions and characteristics and test the proposed method against the plain face and masked face recognition. The proposed method achieves the highest performance results inside periocular recognition (97.53% accuracy for UBIPr-1 and 97.77% accuracy for EYB-P1), masked face recognition (98.11% accuracy), and plain face recognition (98.26% accuracy). The proposed method is robust against glasses occlusion, artificial geometry transformations, Gaussian and salt pepper noise. Comparison with other works in a similar recognition system shows that our proposed curvature best basis method yields the highest performance results.

INDEX TERMS Best basis, curvature, periocular recognition, wavelet packet transform.

I. INTRODUCTION

The periocular region refers to attributes around the eye with rich information [1]. These attributes include eye, eyelids, sclera, eye corner, eyelashes, skin texture, skin color, blood vessel, and eyebrow [2]. Periocular recognition has been developed to help identify individuals due to the rich and unique information around the eye, comparable to a biometric trait [3]. Periocular recognition becomes essential in cases where the system cannot use complete information from the face, for example, when the face is covered with a face mask to prevent disease transmission. The incomplete information about the facial area due to the face mask may reduce the recognition system's performance [4], [5]. In this kind of situation, the periocular features have the potential to contribute to improving recognition performance.

The periocular region, with dense and complex properties, is one of the most discriminating features found on the face, among other facial features, e.g., forehead, cheek, mouth, and

The associate editor coordinating the review of this manuscript and approving it for publication was Zahid Akhtar.

This work is licensed under a Creative Commons Attribution 4.0 License. For more information, see https://creativecommons.org/licenses/by/4.0/

jaw [6]. The other benefits of periocular regions are that they do not require intricate acquisition processes like the ocular region (iris, retinal and conjunctival vasculature) needs [7]. They also can be used to help with disease detection [8]. Moreover, the periocular regions have proven to be sufficiently stable features as compared to the nose, mouth, or full face to facial alterations due to hormone therapy for gender transformations [9].

The big challenge following this statement is choosing the best or most appropriate feature to represent this periocular region in the recognition system. Existing methods commonly used in periocular recognition to extract these periocular region features are global and local descriptors methods. These include local binary pattern (LBP) [6], local binary patterns (LBP), local phase quantization (LPQ), histogram of oriented gradients (HOG), and Weber local descriptor (WLD) [10], gradient orientation histogram (GO), LBP, and scale-invariant feature transform (SIFT) [11]. The dimensional reduction-based such as principal component analysis (PCA) [12] and linear discriminant analysis (LDA) [13] have been evaluated. Multi-resolution analysis methods, such as wavelet-based [14], [15], and scale-space [16], have been employed to evaluate periocular regions. The periocular recognition system has also been tested using feature descriptor methods such as scale-invariant feature transform (SIFT), speeded up robust features (SURF), binary robust invariant scalable keypoints (BRISK), oriented FAST, and rotated BRIEF (ORB) [17], [18], deep learning and neural network-based [19], [20].

This research focuses on multi-resolution analysis to choose the most appropriate periocular feature. The multi-resolution analysis method lets the observer look at details from a different point of view, such as image scaling in the scale-space method and different frequency sub-bands in the discrete wavelet transform. Looking at the finer scale in different frequency bands means more opportunities to find the most distinctive features in the periocular region.

A. LITERATURE REVIEW

A previous study in [15] utilized the discrete wavelet transform (DWT) and combined it with directionally threshold LBP. The proposed method was evaluated on 1.200 periocular images with left and right periocular regions. This work was observed using three orthogonal wavelets with smaller support, i.e., Haar, Daubechies, and Coiflet wavelets. Although the recognition system was successfully built, the works in [15] did not evaluate the complete family of orthogonal and biorthogonal wavelets and did not compare the results against the characteristics of the wavelet.

The work in [14] extracted magnitude responses of complex Gabor filter, reduced the dimension with direct linear discriminant analysis method, and classified it with Parzen probabilistic neural network. In [21], Gabor wavelet descriptor was fused with local phase quantization. Then the dimension was reduced also using the direct linear discriminant analysis method. These descriptors were invariant to blur and uniform illumination changes, but the authors had not tested them against the periocular biometric.

Wavelet transform is both sensitive to translation and rotation [22]. The two significant drawbacks of wavelet transform are lack of shift-invariant and limited directionality [23]. A recent study in [24] evaluated that the wavelet local feature descriptor (WLFD) was invariant to scale, rotation, and translation. They modified and combined the WLFD by generating wavelet pyramids, keypoint localization, and descriptors. Another study in [25] combined a wavelet with the convolutional neural network (WaveCNet) to produce better noise-robustness. In [26], a scale and rotation invariant wavelet feature transform was proposed using a biorthogonal wavelet and combined only two sub-bands with SIFT. The work in [27] employed a self-adjusting generative adversarial network (GAN) and a semi-soft thresholding approach to Gaussian noise removal.

Our recent work [16] employed multi-resolution analysis methods (discrete wavelet transform and scale-space) and combined them with surface curvature. Although the work in [16] produced satisfying results, the information on multi-resolution analysis has been chosen as a static option, and the performance in each multi-resolution point of view was calculated one by one in the recognition system. There has been a gap in the dynamic selection of only the best information from the multi-resolution analysis. It needs to fulfill the requirement of best representing the data from many resolutions or points of view and being able to extract distinctive features.

The best basis algorithm inside the wavelet packet transform (WPT) may provide a solution to this need. On the one hand, it provides the solution to multi-resolution analysis. Better than a typical discrete wavelet transform (DWT), the WPT brings forth more non-overlapping frequency sub-bands. On the other hand, to select the best basis from WPT, the algorithm can be tuned using a specific criterion according to the purpose of the system. Initially, in signal processing, the best basis algorithm employs the minimum additive cost function based on the signal's entropy as the specific criterion. However, in our investigation, a novel criterion based on the curvature with the dynamic design of best basis selection inside WPT further improves the performance results in the periocular recognition system.

The first work by Coifman and Wickerhauser [28] proposed the best basis algorithm in WPT based on the additive cost function using Shannon entropy for signal compression. Since [28], the best basis algorithm has been employed not only for signal compression [29], [30] but also signal processing, feature extraction and classification [31], [32], [33], [34], [35]. Besides the additive cost function in [28], the work in [36] employed geometric means using generalized Rényi entropy. The work in [30] utilized singular value

decomposition for the best basis selection. The work in [37] introduced the Bayesian approach to best basis selection.

The works on the best basis algorithm inside WPT generally consist of criteria of analyzing one-dimensional data for signal processing and one-dimensional and two-dimensional data for compression. To the best of the authors' knowledge, there has been a lack of investigation for the dynamic selection of a single best basis by employing curvature wavelet coefficients. From the previous works, we list some challenges to be overcome in our periocular recognition system:

- The original best basis algorithm creates a set of the best basis selection that may consist of more than one node inside WPT. Because in a two-dimensional image recognition system, one of the goals is to minimize or reduce the extracted features' size, these two contradict each other.
- The initially proposed additive cost function may not be the most suitable criterion for high performance in two-dimensional images on the periocular recognition system.
- Based on the work in [31] and [32], they proposed to use the system's performance from the cross-validation results to select the best basis and later use this best basis that produced the highest performance in the system performance evaluation. This method still needs two steps to find the best basis selection and evaluate the performance. Moreover, the selected best basis is the same for all evaluated data in one cross-validation loop.

To tackle these problems, we propose a novel idea of curvature best basis, i.e., using the statistical measurement of the curvature wavelet coefficients as the criterion of the best basis selection inside WPT. The quad-tree WPT builds a multi-resolution analysis of the data. This multi-resolution analysis based on WPT is not a novel idea. Moreover, the best basis selection from the previous works is generally based on the entropy value. This work utilized the curvature value of the WPT coefficients. The system selects one single WPT coefficient as the best basis to represent the entire periocular region (extracted feature) by calculating the highest standard deviation of the curvature wavelet coefficients.

To answer the problem of the significant drawback inside wavelet transformation, we combine our extracted curvature best basis and the histogram of oriented gradients. To construct a complete analysis, we test the proposed method against variations in wavelet functions, wavelet characteristics, the challenges in artificial geometry transformations (translation, rotation, scaling, shearing, and illumination), artificial Gaussian and salt pepper noise, and the occlusion of wearing glasses in the periocular images.

B. THE CONTRIBUTIONS OF THIS WORK

The key contributions of this work are listed as follows:

- We propose a novel criterion for selecting the best basis based on the highest standard deviation from curvature WPT coefficients.
- The system dynamically selects a single best basis inside WPT as the representation or extracted feature inside the periocular recognition system.
- It is worth noting that each evaluated data may have a different single best basis selection. In our work, the best basis selection is designed for individual data. This idea produces higher performance results in the periocular recognition system.
- We examine the effect of using seven orthogonal wavelets and two biorthogonal wavelets, including wavelet characteristics such as wavelet symmetry, smoothness, number of vanishing moments, and wavelet filter's length.
- We evaluate the curvature best basis method against challenges in artificial geometry transformations (translation, rotation, scaling, shearing, and illumination), artificial noise, and the occlusion of wearing glasses. Our proposed method is robust against these challenges.
- The proposed method is tested against plain and masked face recognition to show the extended ability of the curvature best basis method. The proposed method also shows higher performances in these systems.

II. RELATED THEORY

A. WAVELET PACKET TRANSFORM AND BEST BASIS SELECTION

A wavelet is a short and small wave with zero average value. As a mathematical function capable of shifting and scaling, wavelet aids in helping analyze a signal and assists as an extractor of important information [38], [39]. The wavelet transformation is divided into the continuous wavelet transform and the discrete wavelet transform. While the continuous wavelet transform creates many coefficients in continuous periodic scales and can be used, for example, in the noise removal process [40], the discrete wavelet transform is more suitable for feature extraction. The discrete wavelet transform (DWT), $T_{c,d}$ (1) is the inner product of input signal x and the wavelet function $\psi_{c,d}$ (2) [41]. The values of $T_{c,d}$ are the wavelet coefficients. DWT produces two wavelet coefficients, i.e., a scaling coefficient (approximation coefficient or low frequency component) and a wavelet coefficient (detail coefficient or high frequency component).

$$T_{c,d} = \langle x, \psi_{cd} \rangle \tag{1}$$

$$\psi_{c,d}(t) = \frac{1}{\sqrt{a_0^c}} \psi \left(\frac{t - db_0 a_0^c}{a_0^c} \right) \tag{2}$$

where

c and d control the dilation and translation of the wavelet, respectively,
a_0 is fixed dilation step parameter and $a_0 > 1$,
b_0 is the location parameter and $b_0 > 0$.

The wavelet packet transform (WPT) is an extension of the DWT. The main difference between WPT from DWT is in the total number of coefficients and which coefficient to filter again. In the DWT, only the scaling coefficient is filtered and goes to the next level of decomposition. The WPT passes both scaling and wavelet coefficients to low pass and high pass filters, producing more information than the DWT [42].

Fig. 1 shows the WPT for two levels (*J-1* and *J-2*). With a tree-like structure, where each parent node produces two children for one-dimensional data (binary tree) and four children for two-dimensional data (quad-tree), two levels of quad-tree WPT produce a total of 21 wavelet coefficients (nodes) from $I_{(J,0)}$ to $I_{(J\text{-}2,15)}$. With the same level of decomposition, the DWT only produces a total of 9 wavelet sub-bands, as shown in Fig.1, as red color nodes. We can see from Fig. 1 that DWT is mainly on the left side of the WPT quad-tree.

The LL, LH, HL, and HH indicate the filtering processes for each coefficient, i.e., low pass, downsampled by two, then low pass (LL), low pass, downsampled by two, then high pass (LH), high pass, downsampled by two, then low pass (HL), and high pass, downsampled by two then high pass (HH). Low and high pass filters are adjusted according to the selected wavelet function. In this work, we investigate the orthogonal wavelets, i.e., Haar, Symlet, Daubechies, Coiflet, discrete Meyer, and biorthogonal wavelets, i.e., biorthogonal and reverse biorthogonal wavelet.

The WPT filtering operations for (*J-1*) level are obtained below.

$$I_{(J-1,0)} = \mathrm{LL} I_{(J,0)} \tag{3}$$
$$I_{(J-1,1)} = \mathrm{LH} I_{(J,0)} \tag{4}$$
$$I_{(J-1,2)} = \mathrm{HL} I_{(J,0)} \tag{5}$$
$$I_{(J-1,3)} = \mathrm{HH} I_{(J,0)} \tag{6}$$

The filtering operations for *(J-2)* level of WPT are shown in Table 1 below.

TABLE 1. Filtering operation For *(J-2)* level in WPT.

from $I_{(J\text{-}1,0)}$		from $I_{(J\text{-}1,1)}$	
$I_{(J-2,0)} = \mathrm{LL}\, I_{(J-1,0)}$	(7)	$I_{(J-2,4)} = \mathrm{LL}\, I_{(J-1,1)}$	(11)
$I_{(J-2,1)} = \mathrm{LH}\, I_{(J-1,0)}$	(8)	$I_{(J-2,5)} = \mathrm{LH}\, I_{(J-1,1)}$	(12)
$I_{(J-2,2)} = \mathrm{HL}\, I_{(J-1,0)}$	(9)	$I_{(J-2,6)} = \mathrm{HL}\, I_{(J-1,1)}$	(13)
$I_{(J-2,3)} = \mathrm{HH}\, I_{(J-1,0)}$	(10)	$I_{(J-2,7)} = \mathrm{HH}\, I_{(J-1,1)}$	(14)
from $I_{(J\text{-}1,2)}$		from $I_{(J\text{-}1,3)}$	
$I_{(J-2,8)} = \mathrm{LL}\, I_{(J-1,2)}$	(15)	$I_{(J-2,12)} = \mathrm{LL}\, I_{(J-1,3)}$	(19)
$I_{(J-2,9)} = \mathrm{LH}\, I_{(J-1,2)}$	(16)	$I_{(J-2,13)} = \mathrm{LH}\, I_{(J-1,3)}$	(20)
$I_{(J-2,10)} = \mathrm{HL}\, I_{(J-1,2)}$	(17)	$I_{(J-2,14)} = \mathrm{HL}\, I_{(J-1,3)}$	(21)
$I_{(J-2,11)} = \mathrm{HH}\, I_{(J-1,2)}$	(18)	$I_{(J-2,15)} = \mathrm{HH}\, I_{(J-1,3)}$	(22)

The best basis algorithm is a task-specific algorithm running for some criterion to find the best basis in the WPT according to the purpose and goal of the system. For compression, the purpose is to find the minimized additive cost function. For classification and feature extraction, the best basis algorithm finds the basis that best represents extracted features from the data to improve the performance. The extracted features need to follow two requirements. They need to extract the best representation of a given class of data and create the best distinction between classes [34], [43].

Fig. 2 illustrates the procedure of finding the best basis with the specific criterion of the minimized additive cost function. It is the original algorithm by the work in [28]. The children's nodes are compared with their parent nodes, and the algorithm chooses the one with the minimum cost. If the parent's cost is less than the total of the children's cost, then the algorithm first marks the parent. On the contrary, if the children's costs are less than the parent's, the algorithm updates the parent's cost with the sum of the children's costs. The algorithm works from the bottom nodes *(J-2)* to the top node *(J)*. After all the nodes are compared, the algorithm selects the topmost mark nodes and creates a set of the best basis. An example of the best basis can be a set of $\{I_{(J-1,0)}I_{(J-3,4)}I_{(J-3,5)}I_{(J-2,3)}\}$ (Fig. 2 with blue marks) or a set of $\{I_{(J-2,0)}I_{(J-3,2)}I_{(J-3,3)}I_{(J-1,0)}\}$ (Fig. 2 with red marks).

B. SURFACE CURVATURE

A surface of an image can be seen as a surface in $\mathbb{R}^3$ in a two-dimensional regular submanifold of $\mathbb{R}^3$. Let p be a point of surface S in $\mathbb{R}^3$, a normal vector N_p to S at p is orthogonal to the tangent plane of S. A normal vector of $\mathbf{N_p}$ [44] can be written as

$$\mathbf{N_p} = \sum_{i=1}^{3} a^i(p) \frac{\partial}{\partial x^i}\bigg|_p \tag{23}$$

The intersection $P \cap S$ is a normal section of the surface S through p. The curvature of a normal section with respect to $\mathbf{N_p}$ can be calculated, and the group of curvatures at p of all normal sections represents how the surface curves at p. The unit tangent vector $\mathbf{X_p}$ determines an orientation at normal section. Fig. 3 shows an illustration of the normal vector and tangent vector at p on S. The arclength parametrization of the normal section is $\gamma(s)$, with $\gamma(0) = p$ and $\gamma'(0) = \mathbf{X_p}$. The normal curvature $\kappa\left(X_p\right)$ of $\gamma(s)$ at p is

$$\kappa\left(\mathbf{X_p}\right) = \langle \gamma''(0), \mathbf{N_p} \rangle \tag{24}$$

The set of all unit vectors in the tangent plane of S is a circle, hence a function of κ in (25). The maximum and minimum values of κ_1 and κ_2 of κ are the principal curvatures of surface S at p. The mean curvature H (26) and Gaussian curvature K (27) can be calculated from the principal curvature of κ_1 and κ_2 [45].

$$\kappa : U^1 \longrightarrow \mathbb{R} \tag{25}$$
$$H = \frac{\kappa_1 + \kappa_2}{2} \tag{26}$$
$$K = \kappa_1 \kappa_2 \tag{27}$$

Accordingly, the value of κ_1 and κ_2 are the eigenvalues of the square matrix of the second fundamental form II_{ij} (28).

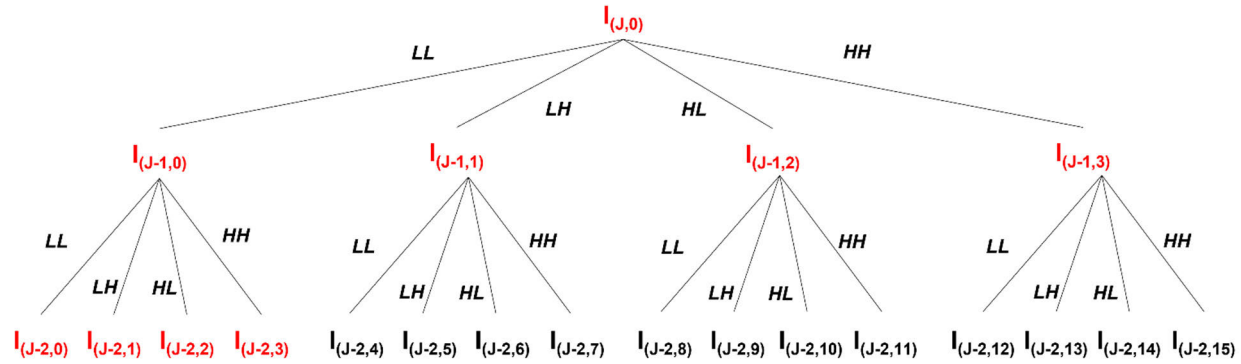

FIGURE 1. The two-dimensional quad-tree wavelet packet transform for image data.

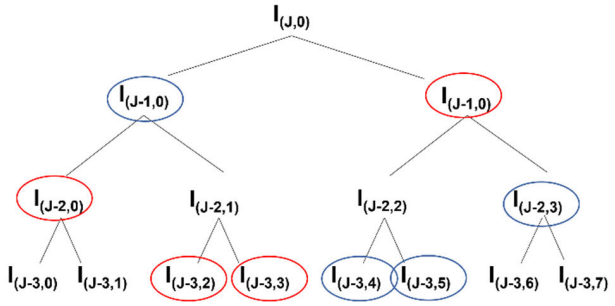

FIGURE 2. The illustration of finding the best basis WPT binary tree based on the minimum additive cost function.

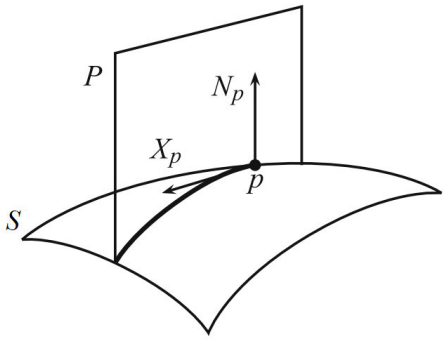

FIGURE 3. The illustration of the normal vector N_p and tangent vector X_p, at point p on surface S [44].

$\mathbf{X_1}$ and $\mathbf{X_2}$ are the tangent vectors at $p$on surface S.

$$II_{ij} = \begin{bmatrix} II(\mathbf{X_1}, \mathbf{X_1}) & II(\mathbf{X_1}, \mathbf{X_2}) \\ II(\mathbf{X_2}, \mathbf{X_1}) & II(\mathbf{X_2}, \mathbf{X_2}) \end{bmatrix} \tag{28}$$

where

$$II\left(\mathbf{X_i}, \mathbf{X_j}\right) = \left\langle \mathbf{X_{ij}}, \mathbf{N_p} \right\rangle \tag{29}$$

and

$$i, j \in \{1, 2\}$$

The mean (H) and Gaussian curvature (K) can also be written as (30) and (31), shown at the bottom of the next page, [45], respectively. with I_{ij} is the first fundamental form

$$I_{ij} = \begin{bmatrix} I(\mathbf{X_1}, \mathbf{X_1}) & I(\mathbf{X_1}, \mathbf{X_2}) \\ I(\mathbf{X_2}, \mathbf{X_1}) & I(\mathbf{X_2}, \mathbf{X_2}) \end{bmatrix} \tag{32}$$

where,

$$I\left(\mathbf{X_i}, \mathbf{X_j}\right) = \left\langle \mathbf{X_i}, \mathbf{X_j} \right\rangle \tag{33}$$

and

$$i, j \in \{1, 2\}$$

C. HISTOGRAM OF ORIENTED GRADIENTS

Histogram of oriented gradients (HOG) is a powerful method that is robust to geometric invariance and image's optical deformation [46]. HOG is also robust to illumination variations in the images. HOG has been employed in many fields, including pedestrian detection, human detection, face recognition, texture classification, car detection, traffic sign detection, crowd density estimation, general object detection, object tracking, feature matching, anomaly detection, and digit recognition [47]. In periocular recognition, HOG and fusion methods using HOG have been producing the best performance results [10], [48], [49].

Popularized by [50], HOG works by calculating the gradient magnitude Mag $(G(x, y))$ and direction Dir $(G(x, y))$ using (34) and (35) respectively. Gradient magnitude and direction are both calculated from the derivative of input matrix M in horizontal $\mathrm{G_x}(x, y)$ and vertical direction $\mathrm{G_y}(x, y)$. Before we calculate the gradient, the input matrix is divided into several blocks (b), and each block is divided into several cells (c).

$$\mathrm{Mag}\left(G(x, y)\right) = \sqrt{\mathrm{G_x}(x, y)^2 + \mathrm{G_y}(x, y)^2} \tag{34}$$

$$\mathrm{Dir}\left(G(x, y)\right) = \tan^{-1}\left(\frac{\mathrm{G_y}(x, y)}{\mathrm{G_x}(x, y)}\right) \tag{35}$$

where

$$\mathrm{G_x}(x, y) = M(x + 1, y) - M(x - 1, y) \tag{36}$$

and

$$\mathrm{G_y}(x, y) = M(x, y + 1) - M(xy - 1) \tag{37}$$

TABLE 2. List of challenges and our proposed solutions.

Previous work	Challenges	Our Proposed Solutions
The original best basis algorithm [28] may create a set of selections of more than one node from WPT.	The set creation contradicts the need for a compact and smaller feature extraction size in the two-dimensional recognition task.	We select only a single node to represent the investigated data.
The criterion of the best basis selection using the additive minimized cost function based on Shannon entropy.	It may not be the most suitable criterion for the two-dimensional image data recognition system.	We propose using curvature value as a novel criterion for the best basis selection.
Based on previous works in [31] and [32], the best basis selection follows the best performance results from cross-validation.	The previous work creates a static selection of the best basis for all data inside one cross-validation loop. The algorithm requires two steps of cross-validation.	A specific and targeted criterion creates a different best basis for each data.
The previous work in [16] generates the multi-resolution analyzed data and can only compare them one by one to select the best feature in the recognition system.	The previous work requires knowing all resolutions' performance and selecting one of the best features.	A dynamic selection of the best basis inside WPT can produce the highest performance results.

This magnitude and direction are then assigned to a histogram with n bins based on the calculated directions. In the end, we have a total of n bins where each bin corresponds to $\frac{360^\circ}{n}$ degrees. The final step is to normalize the histogram of each c within b. HOG features are acquired by concatenating all normalized histogram values of each c within b.

III. THE PROPOSED CURVATURE BEST BASIS METHOD

As mentioned earlier, we have found some challenges from the previous works in the best basis selection inside WPT. Moreover, we ought to implement the best basis algorithm in the two-dimensional periocular recognition system. There is a need to have the best basis selection, which only contains a single node of the best represented extracted feature where each data can be assigned to a different best basis. We intend to fill the gap by enabling the dynamic selection of multi-resolution analyzed data. To explain clearly, we list the previous works, the challenges, and our proposed solutions in Table 2.

We describe the processes inside our proposed method as a schematic block diagram in Fig. 4. The methodology's main processes are summarized in four different schematic blocks, the pre-processing block (blue), WPT and the best basis selection block (green), the HOG block (purple), and the classifier block (orange). The proposed curvature best basis algorithm is displayed as three yellow boxes with red font color in Fig. 4.

The pre-processing (Fig. 4 blue block) consists of two steps, i.e., grayscale image conversion and Gaussian filtering. The input color images $X(m,n)$ are first converted into grayscale images. Then the images are filtered with a Gaussian filter $G_\sigma(mn)$ (38). The approach produces a smoother version of the original image $Y(m,n)$ (39), and this smoothing filter has improved the performance results [16].

$$G_\sigma(m,n) = \frac{1}{2\pi\sigma^2} e^{\frac{-m^2+n^2}{2\sigma^2}} \tag{38}$$

$$Y(m,n) = X(m,n) * G_\sigma(mn) \tag{39}$$

The second part of the proposed method is to build the WPT and select the best basis (Fig. 4 green block). First, we construct the WPT for two levels of decomposition. We build the WPT and stop only for two decomposition levels (Fig. 4 white dashed-box). To go further to more levels may produce lower performance results [16], [31], [32]. Using filters from (3)-(22), we construct 21 WPT coefficients (nodes) with J, $J\text{-}1$, and $J\text{-}2$ and respected τ index as shown in Fig.1.

$$I_{(j,\tau,m,n)} = \{I_{(J,0)}, I_{(J\text{-}1,0)}, \ldots, I_{(J\text{-}2,15)}\} \tag{40}$$

where

$j \in J\text{-}0, J\text{-}1$, and $J\text{-}2$
$0 \leq \tau \leq 15$
$I_{(J,0)} = Y_{(m,n)}$
m and n are the horizontal and vertical locations of the wavelet coefficient

The design of the proposed curvature best basis algorithm (three yellow boxes with red font color inside the green block in Fig. 4) starts from this description. To select a set of the best basis, we do not employ the original criterion to select the best basis using the additive minimal cost function based on entropy. We propose a novel criterion for selecting the best basis using the curvature value. A surface's two most crucial curvature functions are Gaussian and mean curvature [45]. The Gaussian curvature is an intrinsic measure, and the mean curvature is an extrinsic measure [51]. In [16], the extracted curvature that yielded the best performance was derived from the mean curvature. Later in our experiments, we also show that the extracted mean curvature creates more data fluctuations than the Gaussian curvature. These fluctuations are

$$H = \frac{1}{2}\frac{I(\mathbf{X_1},\mathbf{X_1})\,II(\mathbf{X_2},\mathbf{X_2}) - 2I(\mathbf{X_1},\mathbf{X_2})\,II(\mathbf{X_1},\mathbf{X_2}) + I(\mathbf{X_2},\mathbf{X_2})II(\mathbf{X_1},\mathbf{X_1})}{I(\mathbf{X_1},\mathbf{X_1})\,I(\mathbf{X_2},\mathbf{X_2}) - I(\mathbf{X_1},\mathbf{X_2})^2} \tag{30}$$

$$K = \frac{II(\mathbf{X_1},\mathbf{X_1})\,II(\mathbf{X_2},\mathbf{X_2}) - II(\mathbf{X_1},\mathbf{X_2})^2}{I(\mathbf{X_1},\mathbf{X_1})\,I(\mathbf{X_2},\mathbf{X_2}) - I(\mathbf{X_1},\mathbf{X_2})^2} \tag{31}$$

the determinant factor that contributes to creating distinctive features.

To calculate the mean curvature, we derived the X_1 and X_2 from the surface of each element $\in I_{(j,\tau,m,n)}$). To obtain X_1 and X_2, we calculate the first partial derivative from surface S(41). Next, we calculate the first fundamental form using (32) and the second fundamental form using (28). Then we determine the mean curvature using (30).

$$X_{1,2} = \frac{\partial S(m, n, o)}{\partial u, v} \tag{41}$$

where

$S(m, n, o)$ is the surface of wavelet coefficient value of element $\in$ $I_{(j,\tau,m,n)}$
m and n are the horizontal and vertical locations of the wavelet coefficient
o is the wavelet coefficient value

For all elements $\in I_{(j,\tau,m,n)}$, we calculate the mean curvature and create a set of the mean curvature.

$$H_{(j,\tau,m,n)} = \{H_{(J,0)}, H_{(J\text{-}1,0)}, \ldots, H_{(J\text{-}2,15)}\} \tag{42}$$

where

$j \in J\text{-}0, J\text{-}1$, and $J\text{-}2$
$0 \leq \tau \leq 15$
$H_{(J,0)}$ = extracted mean curvature of $Y_{(m,n)}$
m and n are the horizontal and vertical locations of the wavelet coefficient

We have built the WPT and extracted the mean curvature until this step. We also know that the mean curvature shows more fluctuations, which may be the extracted feature that best represents the data. Nevertheless, these have not solved the challenges of dynamically selecting only the single best representation. According to [52], if the choice algorithm is sufficiently cheap, it is possible to assign each data its adapted basis. Intuitively, we know that more fluctuations are good, so how to represent this idea into one single representation that can differ in each data? We introduce the notion of deriving the standard deviation measurement using each element $\in H_{(j,\tau,m,n)}$. The standard deviation (SD) (43) is a measurement of the size of variation or how the data is spread around the mean (μ) (44). The higher standard deviation value indicates more variations around the mean [53].

$$\mathrm{SD} = \sqrt{\frac{1}{mxn-1}\sum_{i=1}^{m}\sum_{j=1}^{n}\left|H_{(i,j)} - \mu\right|^2} \tag{43}$$

with

$$\mu = \frac{1}{mn}\sum_{i=1}^{m}\sum_{j=1}^{n} H_{(i,j)} \tag{44}$$

We calculate the set of the standard deviation (45) for each element $\in H_{(j,\tau,m,n))}$ (42). Based on the intuitive notion that more fluctuations may represent the best data, we choose the highest standard deviation value inside all elements $\in \mathrm{SD}_{(j,\tau)}$. This idea solves the challenge of only using one single node (the dynamical selection of the single best basis) inside WPT, where each data can have a different best basis.

$$SD_{(j,\tau)} = \{SD_{(J,0)}, SD_{(J\text{-}1,0)}, \ldots, SD_{(J\text{-}2,15)}\} \tag{45}$$

where

$j \in J\text{-}0, J\text{-}1$, and $J\text{-}2$
$0 \leq \tau \leq 15$

For all elements $\in \mathrm{SD}_{(j,\tau)}$, we find the one maximum value $\mathrm{SD}_{\max}(p, q)$ (46) and return the index of p and $q$where p indicates the level and q shows the τ in WPT where the $\mathrm{SD}_{\max}$ is located. The curvature best basis (CBB) (47) is the extracted mean curvature $H(p,q,m,n)$with index p and q. The CBB may have a different size for each evaluated data because of the dynamic selection. To tackle this problem, we resize the data according to the mode's (most frequently selected node) size.

$$\mathrm{SD}_{\max}(pq) = \max(\mathrm{SD}_{(j,\tau)}) \tag{46}$$

where

$j \in J\text{-}0, J\text{-}1$, and $J\text{-}2$
$0 \leq \tau \leq 15$
p is J^{th} level where $\mathrm{SD}_{\max}$ located
q is the τ where $\mathrm{SD}_{\max}$ located

$$\mathrm{CBB}(pqmn) = H(pqmn) \tag{47}$$

where

p is J^{th} level where $\mathrm{SD}_{\max}$ located
q is the τ where $\mathrm{SD}_{\max}$ located
m and n are the horizontal and vertical locations of the wavelet coefficient

The third part of the schematic diagram (Fig. 4 purple block) combines the extracted CBB (47) with the histogram of oriented gradients (HOG). We used $c = 8 \times 8$ cells and $b = 2 \times 2$ blocks with $n = 9$ bins for the HOG parameter.

In the last step, we classify the data using the support vector machine (SVM) classifier with a linear kernel (Fig. 4 orange block). Results from [16] show that the linear kernel produced the highest performance compared with the radial basis function (RBF) kernel and the polynomial kernel. The output of the periocular recognition system is performance recognition. We employ a confusion matrix with average accuracy, precision, recall, and F-1 score to evaluate the performance of our proposed method.

IV. EXPERIMENTS, RESULTS, AND DISCUSSION

A. DATASET

1) THE UBIPR PERIOCULAR DATASET [54]

This work evaluates the proposed method using the UBIPr periocular dataset..)()))[54]. The UBIPr dataset is a collection of images of the ocular region on the face and is fit for periocular recognition. The original version of this dataset consists of 11.102 images with 400×300 pixels. The ratio of

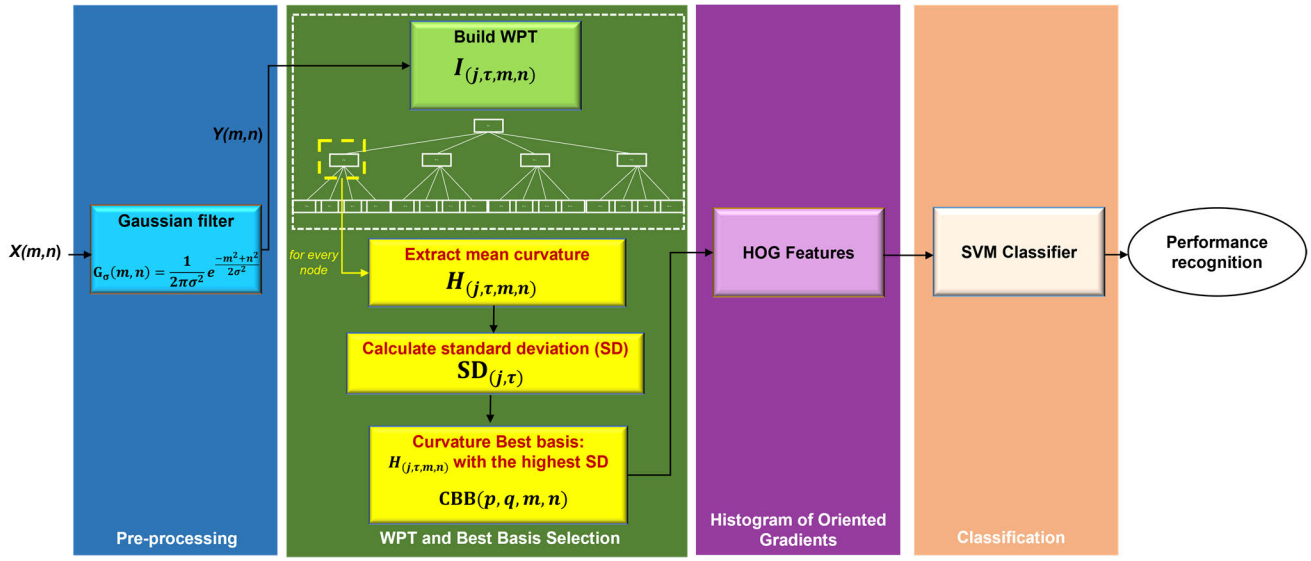

FIGURE 4. The schematic block diagram of the proposed method.

Algorithm 1 Curvature Best Basis

Input: $Y(m, n)$
Output: H[maxIdx]
Declaration:
var I [ ] double
var H [ ] double
var SD [ ] double
var maxIdx int
Initialization:

1: $I \leftarrow$ construct WPT
LOOP Process
2: **for** (idx, element) in I **do**
3: H[idx] $\leftarrow$ extract mean curvature of element
4: SD[idx] $\leftarrow$ calculate standard deviation of H[idx]
5: **end**
6: maxIdx $\leftarrow$ find the idx of max value for (SD)
7: **return** H[maxIdx]

males to females is 54.4:45.6. Volunteers were at large majority Latin caucasian (around 90%), Black (8%), and Asian people (2%). The lighting condition was natural and artificial lighting captured inside a room. The UBIPr dataset has three versions, i.e., the original version, the segmented both eyes version, and the segmented single-eye version. We utilize the segmented both eyes UBIPr dataset version for this work.

To create a balanced dataset, we evaluate images from 217 respondents, with 15 images per respondent. The total number of images is 3.255 images. These periocular images are the ones with no glasses occlusion. The final resized resolution is 30×100 pixels. To evaluate the performance of each region, we divide the periocular region into three, both eye and eyebrow region (UBIPr-1), eye region (UBIPr-2), and eyebrow region (UBIPr-3). Fig. 5 displays the example of these three regions of a UBIPr periocular image.

We also evaluate the robustness of the proposed method by testing against glasses occlusion around the periocular region, artificial geometry transformations, and noise. The UBIPr dataset has images of occlusion with glasses around the periocular regions. From the original dataset, we separate a balanced data sub-set of 27 classes of respondents, each with 15 periocular images with glasses (UBIPr-4). The final resized resolution of UBIPr-4 is 30×100 pixels.

To assess against the artificial geometry and noise challenges, we applied artificial transformations such as rotation, translation, scaling, shearing, added salt and pepper noise, and added Gaussian noise. The rotation is randomly applied between -15 and 15 degrees. The translation randomly adds between 15 pixels to the left or right and the vertical and horizontal location. Salt and pepper noise with a noise density range of 0.15, 0.25, and 0.35 are added for noisy images. The Gaussian noise with a mean range of 0.2 and a variance range of 0.01, a mean range of 0.2 and a variance range of 0.05, a mean range of 0.3 and a variance range of 0.01 is also added to the noise challenges.

For each image inside the UBIPr-1 data sub-set, we develop three rotated images (UBIPr-5), three translated images (UBIPr-6), three scaled images (UBIPr-7), three sheared images (UBIPr-8), three salt-pepper noisy images (UBIPr-9), and three Gaussian noisy images (UBIPr-10). Each artificially created geometry transformation and noise data sub-set (UBIPr-5 – UBIPr-10) has a total of $3.255 \times 3 = 9.765$ images. Fig. 6 shows the example of images inside data sub-set UBIPr-4 until UBIPr-10.

2) THE CROPPED EXTENDED YALE B FACE DATASET [55], [56]

The Cropped Extended Yale B Face Dataset [55], [56] is a face dataset, but for this periocular research, we crop the periocular regions automatically based on the location of the

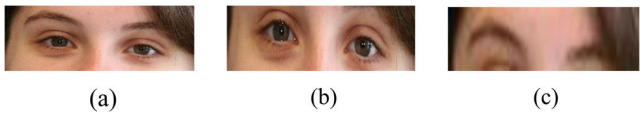

FIGURE 5. Example of images inside (a) UBIPr-1, (b) UBIPr-2, (c) UBIPr-3.

eyes and eyebrows. The dataset has an original 38 frontal face images with 64 variations in pose and lighting angle. The original size of each image is 168×192 pixels in PGM format.

Because some images are too dark, a total of 38 respondents with 59 periocular images per respondent are evaluated. The final resized resolution of the cropped periocular images is 54×168 pixels. To assess the performance of each region, we also divide the periocular regions into three, both eye and eyebrow region (EYB-P1), eye region (EYB-P2), and eyebrow region (EYB-P3).

To analyze the proposed method against plain face recognition, we also utilize the face images inside the cropped extended Yale B face dataset (EYB-F). We employ 38 frontal plain face images with 59 pose and lighting angle variations in each face. The size of the image is 168×192 pixels. Fig. 7 displays the example of the three regions of EYB periocular image (EYB-P1, EYB-P2, and EYB-P3) and the example of EYB plain face (EYB-F).

3) RFFMDS FABRIC MASKED FACE DATASET [57]

The original RFFMDS v 1.0 [57] is a masked face dataset from 8 respondents (three male and five female) with 20 image variations in pose, color, and pattern of the fabric face mask. The lighting condition was artificial lighting captured inside a room. All eight respondents are Asian people. All informed consent from eight respondents was obtained.

To examine the proposed method against the masked face challenge, we expand dan develop the dataset using the artificial geometry transformations and added noise into the RFFMDS v2.0. The RFFMDS v2.0 also has eight respondents, but each respondent provides 1.220 artificial images with variations in poses, colors, pattern fabric face masks, added artificial transformations such as rotation, translation, scaling, shearing, added salt and pepper noise, and added Gaussian noise. The total number of images in the RFFMDS v2.0 is 9.760, with 160 original and 9.600 artificial images.

The rotation was applied randomly between -15 and 15 degrees. The translation was added randomly between 15 pixels to the left or right and the vertical and horizontal locations. Salt and pepper noise with a noise density range between 0.1 and 0.35 are added for noisy images. The Gaussian noise with a mean range between 0.2-0.3 and a variance range between 0.01-0.05 is also added. Ten rotated, ten translated, ten scaled, ten sheared, ten salt and pepper noisy images, and ten Gaussian noisy images are added for each image in the dataset. The final resolution for images is 150×200 pixels. Fig. 8 displays the example of images inside the RFFMDS v2.0 dataset.

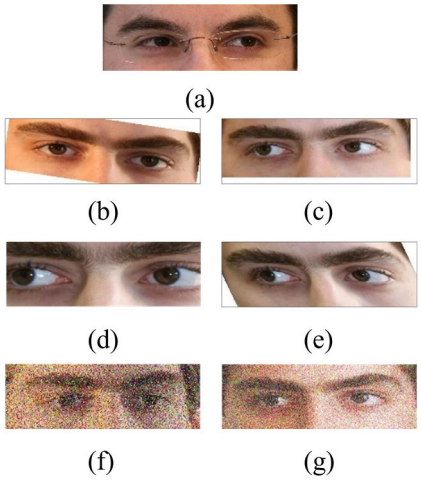

FIGURE 6. Example of images inside (a) UBIPr-4, (b) UBIPr-5, (c) UBIPr-6, (d) UBIPr-7, (e) UBIPr-8, (f) UBIPr-9, (g) UBIPr-10.

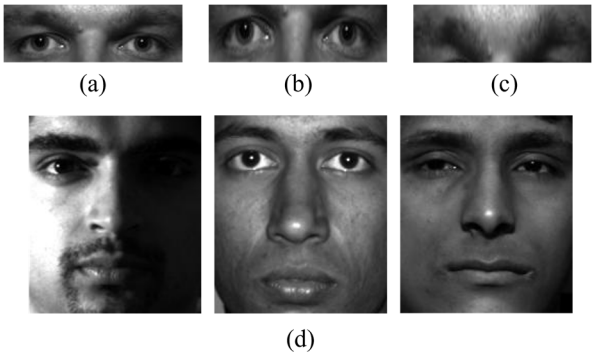

FIGURE 7. Example of images inside (a) EYB-P1, (b) EYB-P2, (c) EYB-P3, and (d) EYB-F.

B. EXPERIMENTAL SETUP

We design several experiments and arrange them to evaluate the proposed curvature best basis method. The list of investigation, experimental setup, results' location, and data sub-sets can be observed in Table 3. First, we test several parameters to be considered inside the curvature best basis, including the statistical measurements, comparison with entropy-based, curvature type, and the selection of single and dynamic. Second, we observe the effect of periocular regions, eye regions, eyebrow regions and using both eye and eyebrow regions. Third, we investigate the effect on seven orthogonal wavelets and two biorthogonal wavelets. Furthermore, we analyze the wavelet characteristics, including wavelet smoothness, number of vanishing moments, wavelet symmetry, and wavelet filter's length. We also calculate running time against the wavelet function.

Fourth, we assess the proposed method for robustness against variations inside the periocular recognition system, including artificial translation, rotation, scaling, and shearing, robustness against Gaussian and salt pepper noise, also occlusion using glasses. To show the extended ability of our proposed method, we examine the curvature best basis against the plain face and masked face recognition. Finally,

FIGURE 8. Example of images inside RFFMDS v2.0.

we compare the results of our work against similar recognition systems.

For all data sub-sets, we train and test all images using 5-fold cross-validation with 20% testing images and 80% training images. Fig. 9 displays the operation inside 5-fold cross-validation. In 5-fold cross-validation, the system first randomly assigns the images into five sections. Each section contains 20% of the total images. In the first fold, the first section (20%) is assigned as the testing data (Fig. 9 red), while the remaining four sections (80%) are assigned as the training data (Fig. 9 blue). In the second fold, the first, third, fourth, and fifth sections are assigned as the training data (Fig. 9 blue), while the second section is assigned as the testing data (Fig. 9 red). The same process happens in the third, fourth, and fifth fold.

All simulations in this work, including the two-dimensional wavelet packet analysis function, the proposed curvature best basis method, histogram of oriented gradients, 5-fold cross-validation, and support vector machine classification, are compiled using MATLAB Version: 9.11.0.1809720 (R2021b) Update 1 running on an Intel (R) Core (TM) i7-7500U CPU @ 2.70GHz, 2.90 GHz processor with 16 GB RAM. The confusion matrix with average accuracy, precision, recall, and F-1 score is employed to evaluate the performance of our proposed method.

C. RESULTS AND DISCUSSION OF THE PROPOSED CURVATURE BEST BASIS METHOD IN THE PERIOCULAR RECOGNITION SYSTEM

1) PARAMETRIC ANALYSIS ON THE PROPOSED CURVATURE BEST BASIS METHOD

We evaluate several parametric analyses to construct our curvature best basis method in the first investigation. For analyzing purposes, we employed the biorthogonal wavelet function (*bior2.2*) for UBIPr-1. We assess the criterion of selecting the best basis based on curvature using the statistical measurements, i.e., mean, correlation, contrast, energy, and standard deviation. The mean (44) corresponds to the average value of the coefficients. The standard deviation (43) measures the spreading of the coefficients around its mean. The correlation shows a relation between one coefficient to others, the contrast calculates differences between coefficients, and energy

TABLE 3. Experimental setup.

Results	Investigation	Data sub-set
C.1)	Parametric analysis on the proposed curvature best basis method in periocular recognition	UBIPr-1
C.2)	Effect of the three periocular regions in periocular recognition	UBIPr-1, UBIPr-2, UBIPr-3, EYB-P1, EYB-P2, EYB-P3
C.3)	Variations in wavelet functions in periocular recognition	UBIPr-1, EYB-P1
C.3)	Effect of wavelet characteristics in periocular recognition and calculation of running time	UBIPr-1, EYB-P1
C.4)	Effect of glasses occlusion around the periocular region in periocular recognition	UBIPr-4
C.4)	Effect of artificial geometry transformations and added noise in periocular recognition	UBIPr-5, UBIPr-6. UBIPr-7, UBIPr-8, UBIPr-9, UBIPr-10
D	Comparison of the proposed method with other works in periocular recognition	
E.1)	Results of the curvature best basis method against plain face recognition	EYB-F
E.1)	Results of the curvature best basis method in masked face recognition	RFFMDS v2.0
E.2)	Comparison of the proposed method with other works in plain and masked face recognition.	

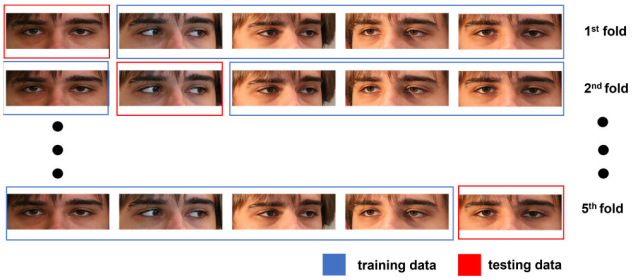

FIGURE 9. The operation inside 5-fold cross-validation.

assesses uniformity and localized changes. The correlation, contrast, and energy measurements can be further studied in [58]. It is worth noting that all statistical measurements are analyzed from the extracted curvature of the WPT node.

Fig. 10 displays the average accuracy of employing these statistical measurements as the single best basis algorithm criterion. We examine the first highest / largest mean, standard deviation, and energy value and the first lowest / smallest value of contrast and correlation. Our intuitive use of standard deviation measurement as the selected criterion is proven. The standard deviation measurement yields the highest performance results of 97.53% compared to other statistical measurements. The standard deviation emphasizes the distinctive feature of the best-represented data on the same class while still strong enough to separate data between classes.

In the following investigation, we compare the entropy-based criteria, i.e., Shannon entropy, threshold, and log entropy, with our proposed criteria. For threshold entropy-based, the threshold value is 0.8, which means the entropy

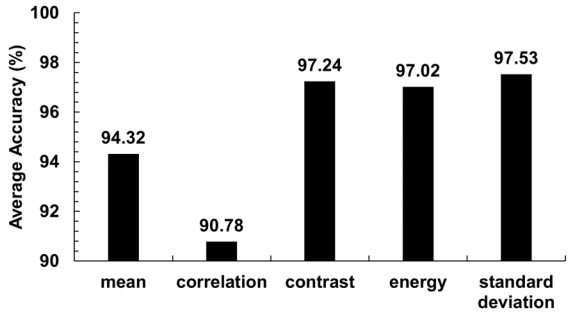

FIGURE 10. Parametric analysis results for criteria on the best basis selection.

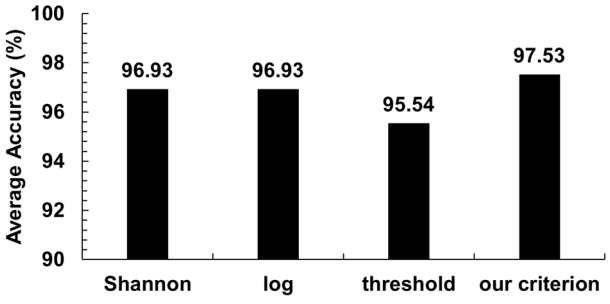

FIGURE 11. Comparison results of our proposed criterion with entropy-based criteria.

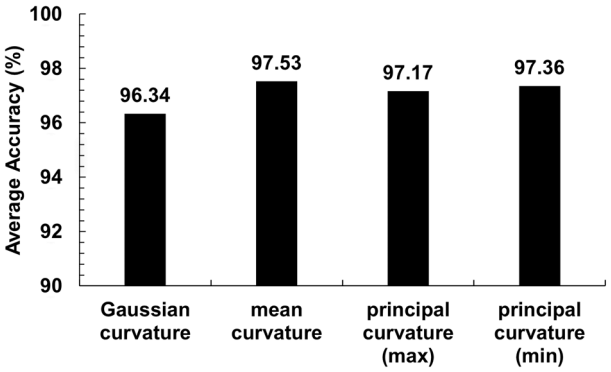

FIGURE 12. Parametric analysis results for different curvature functions.

is calculated below the value of 0.8. The explanation of entropy can be further read in [28] and [59]. We calculate the performance results by selecting the single node inside WPT with the smallest / lowest entropy value. Fig. 11 shows the average accuracy using Shannon entropy, log entropy, threshold, and our proposed criterion. The results show that the initial criteria for using entropy are not giving higher results than our proposed criterion.

In the next analysis, we show why we employ the mean curvature. Fig. 12 shows the average accuracy results from Gaussian curvature, mean curvature, max value of principal curvature, and min value of principal curvature. From [16], we know that the mean curvature has been the best curvature function in terms of performance results. However, we need to analyze the curvature functions further to assess the selection of the best basis algorithm. The results in Fig. 12 support previous work in [16] that the mean curvature achieves the best performance result. Fig. 13 shows the original image, the result of the selected best basis before curvature extraction, the surface plot of Gaussian and mean curvature, and their respective histogram plot. Moreover, we also show in Fig. 13 that the mean curvature (Fig. 13e) produces more fluctuations compared to Gaussian curvature (Fig. 13c). From the histogram plot of both curvature functions (Fig. 13d and Fig. 13f), we see that the mean curvature created more dispersed coefficients around the mean, and it is shown by a higher value of SD of 0.03 compared to SD of Gaussian curvature (0.0017).

We also investigate the results of using the dynamic and static single selection of the best basis. Fig. 14 displays all indexes of the selected best basis. The total data using UBIPr-1 is 3.255 images. From 3.255 single best basis (as our proposed method may assign each data to a different best basis), 52% (1.708 images) are assigned node $I_{(J,0)}$, and 48% (1.547 images) are assigned node $I_{(J\text{-}2,0)}$. Node $I_{(J,0)}$ is the original parent from the WPT. It contains the original Gaussian-filtered images without any process from wavelet transformation. Node $I_{(J\text{-}2,0)}$ is the result of LL filtering from level J to level $J\text{-}1(3)$ and another LL filtering from level $J\text{-}1$ to level $J\text{-}2(7)$. While the first selected node does not have wavelet filtering, the second selected node employs double low pass filtering.

Starting from this information, we further investigate using node $I_{(J,0)}$ and node $I_{(J\text{-}2,0)}$ as the static single best basis. The static single best basis means we assign the same best basis to all data. The results in Fig. 15 emphasize the differences between static and the proposed dynamic single best basis selection. We can see that our proposed dynamic single best basis selection provides the best performance result compared to the static single best basis selection.

2) ANALYSIS OF THREE PERIOCULAR REGIONS

In the second investigation, we observe the effect of the three periocular regions, eyes regions, eyebrows regions, and both eyes and eyebrows regions. Previous works have often investigated the left and right regions of the periocular [15] and the region of interest (ROI) cropped from the periocular regions [60]. The works in [11], [16], [61], and [62] have also investigated the importance of eyebrows in periocular recognition.

To what extent is the effect of employing certain periocular regions, especially using our proposed method, we still need to investigate further. Table 4 displays the average performance results using three periocular regions, i.e., both eyes and eyebrows regions (UBIPr-1, EYB-P1), only eyes regions (UBIPr-2, EYB-P2), and only eyebrows regions (UBIPr-3, EYB-P3). We can see that all data sub-sets (UBIPr-1 and EYB-P1) yield the best results using both eyes and eyebrows regions. We employ the biorthogonal wavelet (*bior2.2*) for the UBIPr dataset and Haar wavelet (*haar*) for the EYB dataset.

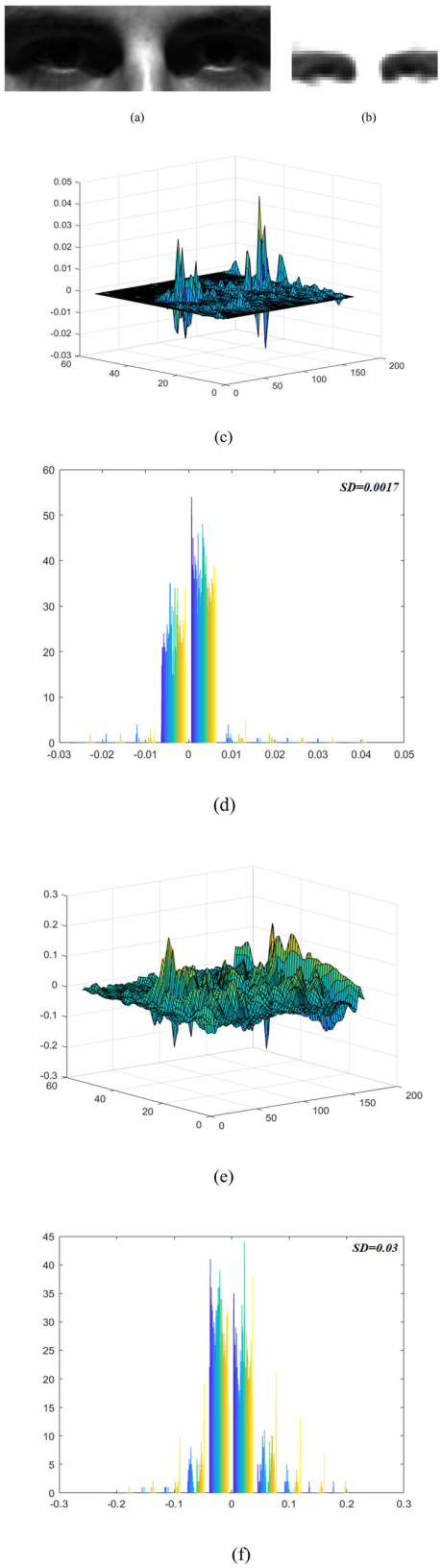

FIGURE 13. a) original periocular image, b) selected best basis before curvature extraction, c) surface plot of extracted Gaussian curvature from (b), d) histogram plot of (c), e) surface plot of extracted mean curvature from (b), f) histogram plot of (e).

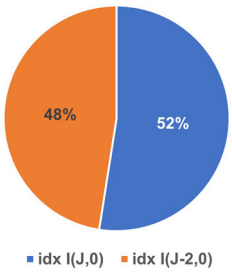

FIGURE 14. The indexes of selected best basis based on the dynamic selection.

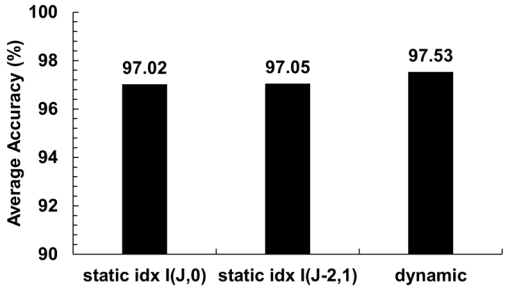

FIGURE 15. Comparison results in the static and dynamic selection of the best basis.

TABLE 4. Average performance results (%) on three periocular regions.

Data Sub-set	Periocular Regions	Accuracy	Precision	Recall	F1-Score
UBIPr-1	both	**97.53**	**97.36**	**97.71**	**97.54**
UBIPr-2	eyes	74.93	74.93	80.05	77.41
UBIPr-3	eyebrows	87.67	87.67	89.61	88.63
EYB-P1	both	**97.77**	**97.77**	**97.86**	**97.82**
EYB-P2	eyes	95.41	95.41	95.71	95.56
EYB-P3	eyebrows	95.99	95.99	96.17	96.08

*The bold indicates the best results.

Table 5 displays the difference in the average accuracy of using certain periocular regions from work in [11] and ours. The work in [11] shows that using the left and right sides of the periocular regions does not affect the recognition system, but if the periocular regions do not include eyebrows, it creates a gap of 10.66% of accuracy difference. In our work, the effect of using eyes regions only (without eyebrows) creates an effect much more significant (22.6% for UBIPr and 2.36% for EYB) than the effect using eyebrows regions only (without eyes) (9.86% for UBIPr and 1.78% for EYB). We conclude that the eyebrows regions significantly affect periocular recognition, and the best region for periocular recognition is using both eyes and eyebrows regions.

3) ANALYSIS OF VARIOUS WAVELET FUNCTIONS AND WAVELET CHARACTERISTICS

We assess the proposed method against various wavelet functions in the third investigation. Seven orthogonal and two biorthogonal wavelet functions are employed to build quadtree WPT. The orthogonal and biorthogonal wavelet functions

TABLE 5. The effect of using certain periocular regions on periocular recognition.

Work (Dataset)	Periocular Regions	Average accuracy difference (%)
[11] (FRGC)	with or without eyebrows	10.66
	both sides or L/R	0.33
ours (UBIPr)	with or without eyebrows	22.60
	with or without eyes	9.86
ours (EYB)	with or without eyebrows	2.36
	with or without eyes	1.78

and their abbreviations (based on the vanishing moments) are presented in Table 6. The orthogonal wavelet has one scaling function and one wavelet function for decomposition and reconstruction, while the biorthogonal wavelet has two pairs, one pair of scaling and wavelet is used for decomposition, and another pair is used for reconstruction.

We start by employing a small number of vanishing moments in each wavelet function in the experiments. A smaller number of vanishing moments helps analyze closely spaced textural features in the images [15], [63]. Therefore, it may be the most suitable parameter choice for periocular regions with dense and complex features. Table 7 shows the properties of wavelet families, including the symmetrical characteristic, the smoothness of the wavelet, the number of vanishing moments, and the filter's length. The symmetrical characteristic is a fixed variable. However, the smoothness, the number of vanishing moments, and the filter's length are not.

Table 8 presents the average performance results for these wavelet functions against two periocular datasets, UBIPr-1 and EYB-P1. The best results are derived from *bior2.2* for UBIPr-1 and *haar* for EYB-P1. The simplest, shortest, and non-smooth Haar wavelet (*haar*) produces the highest results with only one vanishing moment. The Haar wavelet is compact support that has good time localization. It is effective for locating jump discontinuities and efficient representations of signals with small support [59]. At the same time, the biorthogonal wavelet (*bior2.2*) produces the best while having two vanishing moments. The Haar wavelet is antisymmetric, and the biorthogonal wavelets have exact symmetry. Haar and biorthogonal wavelets (with fewer vanishing moments) are non-smooth wavelets. Table 8 shows that the wavelet functions that produce the highest results for both datasets are non-smooth wavelets. The periocular image for both datasets contains abrupt changes, such as the changes when the skin area meets the eyebrows or eyes edges. We can say this condition is where image's region is not smooth. Supported by the experiments' results, the best wavelet functions to analyze these kinds of features are non-smooth wavelet functions.

We also calculate the accuracy against the running time of each wavelet function. Fig. 16 displays the accuracy and running time for each wavelet in UBIPr-1 and EYB-P1. The

TABLE 6. Wavelet family and their abbreviations.

Wavelet	Vanishing moments [63]	Abbreviation
Haar	1	*haar*
Symlet	2	*sym2*
Daubechies	4 (*db4*) 6 (*db6*)	*db4, db6*
Coiflet	2 (*coif1*), 4 (*coif2*)	*coif1, coif2*
discrete Meyer	-	*dm*
biorthogonal	2	*bior2.2*
reverse biorthogonal	2	*rbio2.2*

TABLE 7. Wavelet characteristics.

Wavelet	Symmetry [39]	Vanishing moment [63]	Smooth [39]	Filter's length [39]
haar	anti sym	1	no	2
sym2	near sym	(Ψ)=2	if N large	(2N) = 4
db4, db6	not sym	*db4*, (Ψ)=4 *db6*, (Ψ)=6	if N large	*db4*, (2N) = 8 *db6*, (2N) = 12
coif1, coif2	near sym	*coif1*, (Ψ / Φ)=2 *coif2*, (Ψ / Φ)=4	if N large	*coif1*, (6N)=6 *coif2*, (6N)=12
dm	yes	-	yes	-
bior2.2	exact	(Nr)=2	if N large	max(2Nr,2Nd)+2 = 6
rbio2.2	exact	(Nd)=2	if N large	max(2Nr,2Nd)+2 = 6

N = wavelet order, Ψ = wavelet function, Φ= scaling function, Nr = reconstruction filter, Nd = decomposition filter

running time is calculated from one image to be processed in the pre-processing, WPT and proposed curvature best basis, and histogram of oriented gradients. From Fig. 16, we observe that the average running time is approximately 0.8 seconds. For both datasets, discrete Meyer (*dm*) is the wavelet that produces the longest running time and has the lowest accuracy results. The computation complexity of our proposed curvature best basis is O(n).

In the following investigation, we observe the number of vanishing moments and the length of the wavelet filter. According to Table 7, these wavelet characteristics are connected. The larger number of vanishing moments produces a longer filter's length and smoother wavelet function. We investigate these wavelet's characters and discover the effect on the performance results. The average accuracy results are shown in Table 9 and Fig. 17. From previous results in Table 8, we know that *haar* wavelet (length=2) yields the best for EYB-P1 (97.77%) and the *bior2.2* wavelet (length=6) for UBIPr-1 (97.53%). However, after we analyze the wavelet functions based on the length, the *rbio4.4* (length=10) shows better performance results for both datasets (97.54% for UBIPr-1 and 97.99% for EYB-P1). Nevertheless, the improvement is insignificant (0.01% for UBIPr-1 and 0.22% for EYB-P1), and the filter's length is much longer. The average accuracy results show decrement for both datasets starting from length = 20 and decreasing until length = 80. Fig. 18 displays the low pass and

TABLE 8. Average performance results (%) on various wavelet functions.

Wavelet	Data subset	Accuracy	Precision	Recall	F1-Score
haar	UBIPr-1	97.38	97.05	97.48	97.26
	EYB-P1	**97.77**	**97.77**	**97.86**	**97.82**
sym2	UBIPr-1	97.43	97.33	97.79	97.56
	EYB-P1	97.55	97.55	97.66	97.60
db4	UBIPr-1	97.22	97.05	97.56	97.30
	EYB-P1	97.15	97.15	97.26	97.20
db6	UBIPr-1	97.39	97.08	97.47	97.27
	EYB-P1	96.65	96.65	96.79	96.72
coif1	UBIPr-1	97.50	97.30	97.66	97.48
	EYB-P1	97.59	97.59	97.69	97.64
coif2	UBIPr-1	97.07	97.05	97.55	97.30
dm	UBIPr-1	93.07	92.75	94.12	93.43
	EYB-P1	84.39	84.39	85.48	84.93
bior2.2	UBIPr-1	**97.53**	**97.36**	**97.71**	**97.54**
	EYB-P1	97.68	97.68	97.76	97.72
rbio2.2	UBIPr-1	96.91	96.74	97.10	96.92
	EYB-P1	97.55	97.55	97.66	97.60

*The bold indicates the best results.

high pass filter of *db10* (length=20), *db20* (length 40), and *db40* (length80). While the performance decreases, the system takes more running time to do the filtering when we use the longer filter's length. We can conclude from these investigations that the most suitable characteristics of wavelet functions in the periocular recognition system are the non-smooth wavelet, with small vanishing moments and a short filter's length.

We also compare the results of our proposed curvature best basis method with discrete wavelet transform (DWT) and WPT nodes. In this comparison, we only extract DWT and WPT coefficients and directly classified them with SVM. The DWT is employed using one level of decomposition and approximation sub-band. The WPT nodes are selected as static single node from node $I_{(J\text{-}2,4)}$ for *haar,* node $I_{(J\text{-}2,1)}$ for *sym2*, node $I_{(J\text{-}2,0)}$ for *db4*and *db6*, node $I_{(J\text{-}2,1)}$ for *coif1* and *coif2*, node $I_{(J\text{-}2,0)}$ for *dm*, and node $I_{(J\text{-}2,1)}$ for *bior2.2* and *rbio2.2*. The choice of approximation sub-bands for DWT and selected nodes for WPT because they produce the best results compared to other sub-bands for DWT and nodes for WPT. Fig. 19 displays the comparison results, and we can see that our proposed curvature best basis yields the best results. It improves 29.8% from DWT and 28,5% from WPT for *bior2.2*.

4) EXPERIMENT RESULTS ON GLASSES OCCLUSION, ARTIFICIAL GEOMETRY TRANSFORMATION, AND NOISE CHALLENGES

In this investigation, we analyze the proposed curvature best basis method and its robustness against various challenges

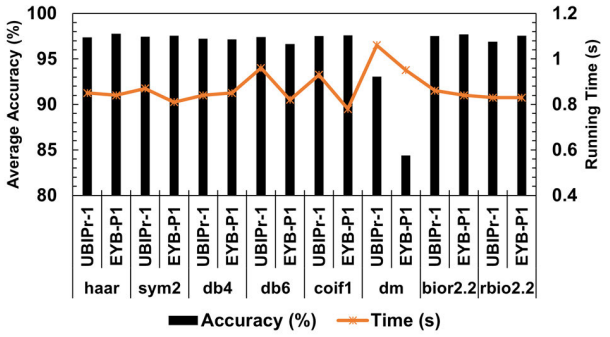

FIGURE 16. Average accuracy (%) and the running time (s) of UBIPr-1 and EYB-P1 against wavelet functions.

TABLE 9. Average accuracy (%) on the effect of wavelet filter's length.

Vanishing moment	Filter's length	Wavelet	UBIPr-1	EYB-P1
1	2	*haar*	97.38	**97.77**
2	4	*sym2*	97.43	97.55
2	6	*bior2.2*	**97.53**	**97.68**
4	8	*db4*	97.22	97.15
4	10	*rbio4.4*	**97.54**	**97.99**
6	12	*db6*	97.39	96.65
6	18	*rbio6.8*	**97.54**	97.32
10	20	*db10*	97.08	95.76
20	40	*db20*	95.55	92.64
40	80	*db40*	92.63	87.95

*The bold indicates the critical findings.

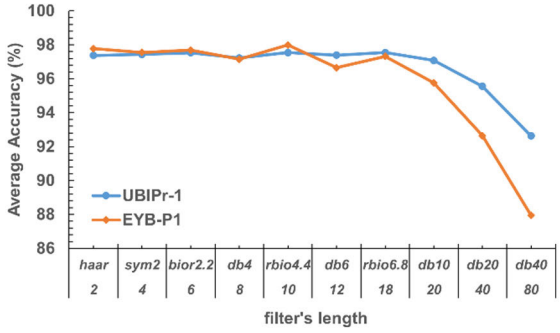

FIGURE 17. Average accuracy (%) with various wavelet filter's lengths evaluated against UBIPr-1 and EYB-P1.

inside periocular recognition. Table 10 shows the performance results of this investigation. Using UBIPr-4, we examine against glasses occlusions around the periocular regions. This challenge slightly improves the performance results by 0.34% of average accuracy. We can consider that glasses occlusion does not reduce the recognition system's performance. The work in [3] also stated that the effect of the glasses on periocular recognition did not have much effect.

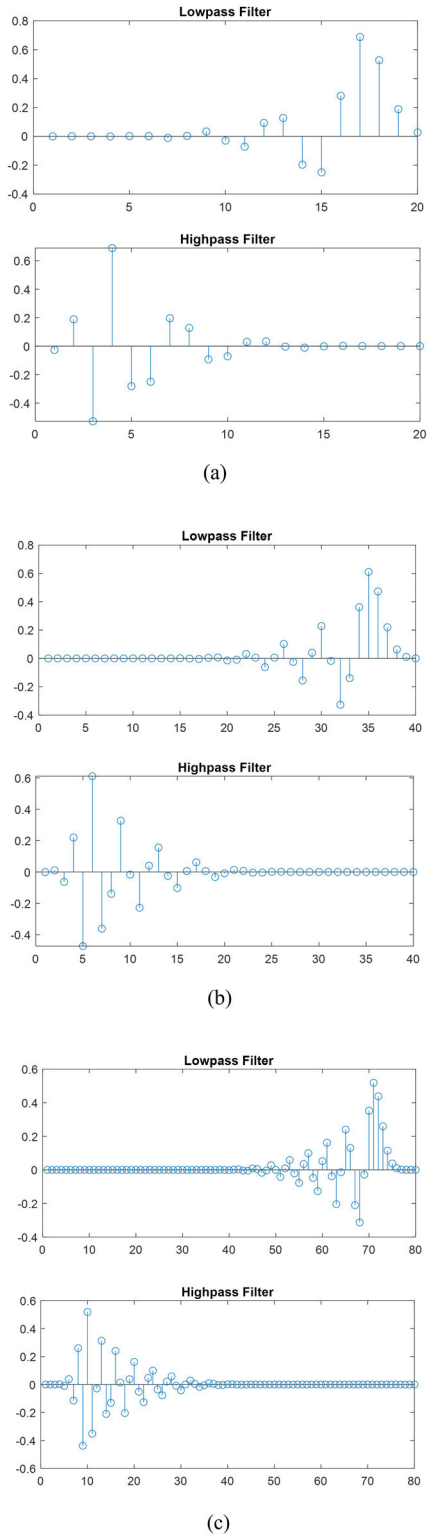

FIGURE 18. Low pass and high pass filter of (a) db10, (b) db20, and (c) db40.

The rotation (UBIPr-5) and translation (UBIPr-6) challenges decrease the results by approximately 1.22% and 5% of average accuracy. In contrast, the scaling (UBIPr-7) and shearing (UBIPr-8) improve the results by 1.02% and 1.27%

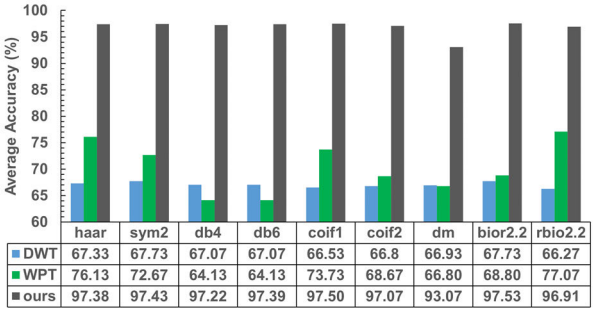

	haar	sym2	db4	db6	coif1	coif2	dm	bior2.2	rbio2.2
DWT	67.33	67.73	67.07	67.07	66.53	66.8	66.93	67.73	66.27
WPT	76.13	72.67	64.13	64.13	73.73	68.67	66.80	68.80	77.07
ours	97.38	97.43	97.22	97.39	97.50	97.07	93.07	97.53	96.91

FIGURE 19. Comparison of average accuracy (%) results from UBIPr-1 data sub-set between DWT, WPT, and our proposed method.

of average accuracy. The scaling process may crop out skin area on periocular images and focus on certain periocular features. The image's pixel location changes in the shearing transformation, but the horizontal and vertical structure is preserved [64]. This may be why the scaling and shearing challenges do not reduce the recognition performance but improve them. Adding salt and pepper noise to periocular images (UBIPr-9) significantly lowers the performance but adding Gaussian noise does not lower the performance and improves 0.64% of average accuracy.

Wavelet transform is both sensitive to translation and rotation [22]. Adding noise also affects the performance of the recognition system. Table 11 emphasizes the difference in average accuracy results based on the WPT method (Fig. 19) and our proposed curvature best basis method on various challenges. We can see that the rotation and translations are reduced by 39.07% and 71.74% using WPT nodes. Our proposed curvature best basis method only reduces 1.22% and 5% for rotation and translation challenges. Unfortunately, adding salt and pepper noise on periocular images still significantly reduces 19.16% the accuracy performance of the curvature best basis method.

To see the effect on how much the quality of periocular images is reduced, we calculate the structural similarity index (SSIM) for UBIPr-5 (rotation), UBIPr-6 (translation), UBIPr-7 (scaling), and UBIPr-8 (shearing). We also compute peak signal-to-noise-ratio (PSNR) for UBIPr-9 (salt and pepper noise) and UBIPr-10 (Gaussian noise). Due to the random degree of artificial geometry transformations and noise, we calculate SSIM and PSNR as average values. Fig. 20a displays the relation between average accuracy and SSIM of various challenges, and Fig. 20b displays the relation between average accuracy and PSNR of Gaussian and salt pepper noise. The lower SSIM value means a higher degradation of the transformed image. The higher PSNR value means a better quality of the noisy image. From Fig. 20a, we observe that the lowest SSIM value (0.46) between artificial geometry transformation comes from scaling. However, our proposed method yields 98.55% of accuracy. The Gaussian and salt pepper noisy images' SSIM values are 0.27 and 0.09, respectively. The accuracy of the recognition system when we use Gaussian noisy images is 98.17%, and 78.37% when salt

TABLE 10. Average performance results (%) on different challenges.

Data sub-set	challenge	Accu-racy	Preci-sion	Recall	F1-Score
UBIPr-1	no challenge	97.53	97.36	97.71	97.54
UBIPr-4	glasses	**97.87**	**97.87**	**98.23**	**98.05**
UBIPr-5	rotation	96.31	96.31	96.60	96.46
UBIPr-6	translation	92.53	92.53	93.54	93.03
UBIPr-7	scaling	**98.55**	**98.55**	**98.65**	**98.60**
UBIPr-8	shearing	**98.80**	**98.80**	**98.84**	**98.82**
UBIPr-9	noise salt and pepper	78.37	78.37	83.90	81.04
UBIPr-10	noise Gaussian	**98.17**	**98.17**	**98.29**	**98.23**
EYB-P1	illumination	97.77	97.77	97.86	97.82

* The bold indicates essential findings.

TABLE 11. Comparison of average accuracy differences (%) on WPT and our proposed method against various challenges.

challenge	WPT	ours
rotation	39.07	1.22
translation	71.74	5
salt and pepper noise	2.07	19.16
Gaussian noise	1.74	-

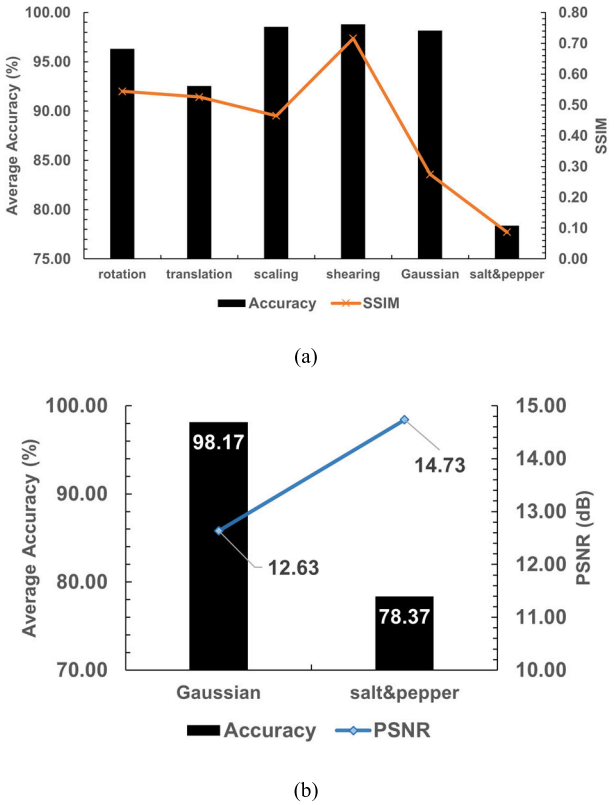

FIGURE 20. a) Average accuracy vs average SSIM on various challenges, b) Average accuracy vs average PSNR of Gaussian and salt pepper noise.

and pepper noise is employed. Moreover, from Fig. 20b, we observe that the PSNR value is 12.63 dB for Gaussian noisy images and 14.73 dB for salt pepper noisy images. From these results, we can infer that the reduced performance in UBIPr-9 (salt and pepper noise) is due to high degradation with SSIM 0.09 and PSNR 14.73 dB.

D. COMPARISON WITH OTHER WORKS OF PERIOCULAR RECOGNITION

In this section, we compare the proposed curvature best basis method's performance to other works for periocular recognition. Table 12 presents the comparison using the best accuracy. The work in [6] employed interpolated local binary pattern (ILBP), while in [65] employed generalized label smoothing regularization (GLSR). In [14], they combined Gabor filters with direct linear discriminant analysis (DLDA) and classified them with Parzen probabilistic neural network (PPNN). The work in [60] utilized rectangular region of interest (ROI) and VGG19 architecture for CNN. Four subregions are extracted with KAZE, HOG, and SING feature extraction methods and naïve Bayes classifier utilized in [66]. In [3], CNN, HOG, and gender information (GI) were employed. The work in [67] investigated rotation invariant uniform LBP and color moment while in [48] used higher order spectral (HOS) features based on an elliptical coordinate sampling. In [17], they combined feature extraction methods such as SIFT, SURF, LBP, BRISK, and ORB. Table 12 shows that our proposed curvature best basis method performs better than previous works.

E. RESULTS AND DISCUSSION OF THE PROPOSED CURVATURE BEST BASIS METHOD IN PLAIN FACE AND MASKED FACE RECOGNITION

1) EXPERIMENT RESULTS ON PLAIN AND MASKED FACE RECOGNITION

To show the effectiveness of the curvature best basis method, we assess the proposed method against plain and masked face recognition. Table 13 displays the results on plain face recognition using EYB-F and masked face recognition using RFFMDS v2.0. The evaluations also consider the various wavelet functions. Using the curvature best basis method, we achieve 98.26% accuracy for plain face recognition with *coif1*, *bior2.2*, *rbio2.2*, and 98.11% for masked face recognition with *dm*. In plain face recognition, *coif1*, *bior2.2*, and *rbio2.2*have filter's length equal to 6. *Coif1* is near symmetry, while both *bior2.2* and *rbio2.2* have exact symmetry. In masked face recognition, *dm*is a smooth and symmetrical wavelet.

We also examine the indexes of all selected best basis for plain face and masked face recognition. From 2.242 single best basis using EYB-F, 61% (1.359 images) are assigned node $I_{(J,0)}$, and 39% (883 images) are assigned node $I_{(J-2,0)}$. On the contrary, from 9.760 single best basis using RFFMDS v2.0, 48% (4.649 images) are assigned node $I_{(J,0)}$, and 52%

TABLE 12. Performance comparison with other works of periocular recognition.

Method	Dataset*	Best Accuracy (%)
ILBP [6]	UBIPr	78.3
GLSR [65]	ETHNIC, PUBFIG, FACE-SCRUB, IMDB WIKI	88.7
Gabor+DLDA+PNN [14]	PUT	89.7
Rectangular ROI + VGG19 [60]	UBIPr	90
4 subregions + KAZE + HOG + SING + naïve Bayes [66]	UBIPr	92.32
CNN + HOG + GI [3]	UBIPr	93.83
rotation invariant uniform LBP and color moment [67]	UBIPr	95.9
HOS + elliptical sampling [48]	FRGC	95.96
SURF + SIFT, LBP + SURF, SIFT, SURF, ORB, BRISK [17]	FERET	96.8
curvature best basis (CBB)	**EYB**	**97.77**
curvature best basis (CBB)	**UBIPr**	**97.53**

*If the dataset is a face dataset, then the works only use periocular regions. The bold indicates the results of our proposed method.

TABLE 13. Average performance results (%) on plain and masked face recognition using the curvature best basis method.

Data subset	Wavelet	Accuracy	Precision	Recall	F1-Score
EYB-F	*haar*	98.22	98.22	98.25	98.24
	sym2	98.22	98.22	98.27	98.24
	db4	98.08	98.08	98.15	98.12
	db6	98.17	98.17	98.22	98.20
	coif1	**98.26**	**98.26**	**98.32**	**98.29**
	coif2	98.22	98.22	98.29	98.25
	dm	94.96	94.96	95.21	95.08
	bior2.2	**98.26**	**98.26**	**98.31**	**98.29**
	rbio2.2	**98.26**	**98.26**	**98.32**	**98.29**
RFFMDS v2.0	*haar*	95.42	95.42	95.48	95.45
	sym2	95.69	95.69	95.76	95.72
	db4	95.57	95.57	95.65	95.61
	db6	95.89	95.89	95.95	95.92
	coif1	95.68	95.68	95.75	95.71
	coif2	95.90	95.90	95.96	95.93
	dm	**98.11**	**98.11**	**98.13**	**98.12**
	bior2.2	95.42	95.42	95.50	95.46
	rbio2.2	95.92	95.92	95.99	95.96

*The bold indicates the best results

(5.111 images) are assigned node $I_{(J\text{-}2,0)}$. Although the proposed method yields high results, using periocular images from the same dataset (97.77% from EYB-P1) almost surpasses the recognition system that employs plain face images (98.26% from EYB-F). The proposed curvature best basis method also shows robustness against the occluded face especially using a fabric face mask with different patterns and colors.

TABLE 14. Performance comparison with other works of face recognition using EYB face dataset.

Method	Best Accuracy (%)
ROMCA-2DPCA [68]	69.08
ELGHP [70]	75
JOSedRVFL [71]	80.47
LGHP [69]	84.71
log + DTCWT [72]	92.46
directional gradient maps [73]	95.4
FDPR [74]	95.62
QRCP [75]	97.02
curvature best basis (CBB)	**98.26**

*The bold indicates the result from our proposed method.

TABLE 15. Performance comparison with other works of masked face recognition.

Method	Dataset	Mask Type	Best Accuracy (%)
ArcFace [76]	c-RMFRD$_0$	real	67.8 (R1)
			83.5 (R5)
GLCM + curvature [57]	RFFMDSv1	real	87.5
CNN + MLP [77]	RMFRD	real	91.3
	SMFRD	artificial	88.9
cropping + CBAM [78]	Masked Webface	artificial	91.53
R34-AMaskNet [79]	RMFRD	real	94.3
attention mechanism neural network [80]	RMFRD	real	95.22
	SMFRD	artificial	95.31
curvature best basis (CBB)	**RFFMDSv2**	**real**	**98.11**

*The bold indicates the result from our proposed method.

2) COMPARISON WITH OTHER WORKS OF FACE AND MASKED FACE RECOGNITION

In the final investigation, we compare the proposed curvature best basis method against other works in plain face recognition that employ the same EYB face dataset. Table 14 shows the comparison results. The work in [68] employed robust optimal mean cosine angle 2DPCA (ROMCA-2DPCA). In [69], local gradient hexa pattern (LGHP) and extended version of Local Gradient Hexa Pattern (ELGHP) were investigated [70]. The work in [71] proposed a jointly optimized learning strategy for the edRVFL network (JOSedRVFL). The work in [72] utilized the logarithm domain for the dual-tree complex wavelet transform (DTCWT). In [73], the work used directional gradient maps. A novel fuzzy discriminative projection and representation learning (FDPR) method for classification was proposed in [74]. The work in [75] used orthogonal triangular with column pivoting (QRCP). The proposed curvature best basis method performs the best when compared to these previous works.

We also compare the performance of our proposed method with other works in masked face recognition. The type of face mask is distinguished into a real face mask and an artificial face mask (synthetically created by simulations from plain face images). Table 15 shows the comparison results. In [76], the ArcFace was evaluated against the modified real dataset RMFRD. The work in [57] employed the gray level co-occurrence matrix (GLCM) method and combined it with curvature. They tested against the real dataset RFFMDS v1.0. In [77], occlusion-free facial region images in artificial dataset SMFRD and real dataset RMFRD were evaluated with deep CNN and classified using multilayer perceptron (MLP). The work in [78] employed a cropping-based approach and Convolutional Block Attention Module (CBAM). An attention-aware masked face recognition-based method (R34-AMaskNet) was proposed and tested using RMFRD in [79]. The work in [80] utilized an algorithm based on an attention mechanism neural network and examined them with the real dataset RMFRD and artificial dataset SMFRD. Our proposed curvature best basis method still executes better than other works in masked face recognition.

V. CONCLUSION

This work proposes a novel criterion using the statistical measurement from curvature wavelet coefficient to select a dynamically single best basis inside WPT. The criterion of using the highest standard deviation from curvature wavelet coefficients provides the most distinctive extracted feature that improves recognition's performance. Furthermore, this proposed criterion enables dynamic selection, which yields different single best basis for each evaluated data. The proposed curvature best basis shows the best performance results inside periocular recognition (97.53% accuracy for UBIPr-1 and 97.77% accuracy for EYB-P1), masked face recognition (98.11% accuracy), and plain face recognition (98.26% accuracy). The periocular region that provides the best recognition system performance comes from both eye and eyebrow regions. The proposed method is tested for various wavelet functions and characteristics. The results show that using a non-smooth, small vanishing moment with a short filter length yields the best results. The curvature best basis method is robust against glasses occlusion, scaling, shearing, and Gaussian noise. The rotation and translation challenge slightly lowered the performance results. Comparison with other works in a similar recognition system displays that our proposed curvature best basis performs the best.

Although our work has started the dynamic selection of the best basis, it has not been able to select only one wavelet function. Future works may also consider the wavelet functions that can be dynamically selected inside the wavelet best basis algorithm. The proposed curvature best basis is robust against the scaling and shearing artificial transformation. The scaling and shearing transformations inside the images may be further studied on the extracted features because they have the potential to improve recognition performance. The added noise and artificial geometry transformations can be assessed further by observing an individual range of each added noise and artificial transformation. The effect of running time against noise level range, the effect of resizing images, and its impact on the recognition performance can be further examined.

ACKNOWLEDGMENT

The author Regina Lionnie thanks Ray Djajadinata, Riko Boestari, and Leonard Raymond Setiabudhi for their valuable help in assisting manuscript writing and computer simulations. All authors thank the reviewers and editors for their insight and suggestions.

REFERENCES

[1] P. Kumari and K. R. Seeja, "Periocular biometrics: A survey," *J. King Saud Univ.-Comput. Inf. Sci.*, vol. 34, no. 4, pp. 1086–1097, Apr. 2022, doi: 10.1016/J.JKSUCI.2019.06.003.

[2] G. Kumar, M. A. Zaveri, S. Bakshi, and P. K. Sa, "Who is behind the mask: Periocular biometrics when face recognition fails," in *Proc. 2nd Int. Conf. Power, Control Comput. Technol. (ICPCT)*, Mar. 2022, pp. 1–6, doi: 10.1109/ICPC2T53885.2022.9777027.

[3] P. Kumari and K. R. Seeja, "A novel periocular biometrics solution for authentication during COVID-19 pandemic situation," *J. Ambient Intell. Humanized Comput.*, vol. 12, no. 11, pp. 10321–10337, Nov. 2021, doi: 10.1007/S12652-020-02814-1.

[4] N. Damer, J. H. Grebe, C. Chen, F. Boutros, F. Kirchbuchner, and A. Kuijper, "The effect of wearing a mask on face recognition performance: An exploratory study," in *Proc. Int. Conf. Biometrics Special Interest Group (BIOSIG)*, 2020, pp. 1–6.

[5] D. J. Carragher and P. J. B. Hancock, "Surgical face masks impair human face matching performance for familiar and unfamiliar faces," *Cognit. Res., Princ. Implications*, vol. 5, no. 1, pp. 1–15, Dec. 2020, doi: 10.1186/s41235-020-00258-x.

[6] G. Kumar, S. Bakshi, P. K. Sa, and B. Majhi, "Non-overlapped blockwise interpolated local binary pattern as periocular feature," *Multimedia Tools Appl.*, vol. 80, no. 11, pp. 16565–16597, May 2021, doi: 10.1007/s11042-020-08708-w.

[7] Y. Martinez-Diaz, H. Mendez-Vazquez, L. S. Luevano, M. Nicolas-Diaz, L. Chang, and M. Gonzalez-Mendoza, "Towards accurate and lightweight masked face recognition: An experimental evaluation," *IEEE Access*, vol. 10, pp. 7341–7353, 2022, doi: 10.1109/ACCESS.2021.3135255.

[8] R. A. Ramlee, A. R. Ramli, M. Hanafi, Z. M. Noh, and A. Khmag, "Classification of eye abnormality using statistical parameters in texture features of corneal arcus image," *Adv. Sci. Lett.*, vol. 24, no. 6, pp. 4063–4069, Jun. 2018.

[9] G. Mahalingam, K. Ricanek, and A. M. Albert, "Investigating the periocular-based face recognition across gender transformation," *IEEE Trans. Inf. Forensics Security*, vol. 9, no. 12, pp. 2180–2192, Dec. 014, doi: 10.1109/TIFS.2014.2361479.

[10] K. K. Kumar and P. T. Rao, "Periocular region based biometric identification using the local descriptors," *Adv. Intell. Syst. Comput.*, vol. 673, pp. 341–351, Jan. 2018, doi: 10.1007/978-981-10-7245-1_34.

[11] U. Park, R. Jillela, A. Ross, and A. K. Jain, "Periocular biometrics in the visible spectrum," *IEEE Trans. Inf. Forensics Security*, vol. 6, no. 1, pp. 96–106, Mar. 2011, doi: 10.1109/TIFS.2010.2096810.

[12] S. Alkhazali and M. El-Bashir, "Local binary pattern method (LBP) and principal component analysis (PCA) for periocular recognition," *Int. J. Adv. Comput. Sci. Appl.*, vol. 11, no. 8, pp. 1–7, 2020.

[13] A. Joshi, A. Gangwar, R. Sharma, and Z. Saquib, "Periocular feature extraction based on LBP and DLDA," *Adv. Intell. Soft Comput.*, vol. 166, pp. 1023–1033, May 2012, doi: 10.1007/978-3-642-30157-5_101.

[14] A. Joshi, A. Gangwar, R. Sharma, A. Singh, and Z. Saquib, "Periocular recognition based on Gabor and Parzen PNN," in *Proc. IEEE Int. Conf. Image Process. (ICIP)*, Oct. 2014, pp. 4977–4981, doi: 10.1109/ICIP.2014.7026008.

[15] K. C. Kumar, A. Lala, R. Vyas, and M. Sharma, "Periocular recognition via effective textural descriptor," in *Proc. IEEE 7th Uttar Pradesh Sect. Int. Conf. Electr., Electron. Comput. Eng. (UPCON)*, Nov. 2020, pp. 1–6, doi: 10.1109/UPCON50219.2020.9376575.

[16] R. Lionnie, C. Apriono, and D. Gunawan, "Eyes versus eyebrows: A comprehensive evaluation using the multiscale analysis and curvature-based combination methods in partial face recognition," *Algorithms*, vol. 15, no. 6, p. 208, Jun. 2022, doi: 10.3390/A15060208.

[17] Ş. Karahan, A. Karaöz, Ö. F. Özdemir, A. G. Gü, and U. Uludag, "On identification from periocular region utilizing SIFT and SURF," in *Proc. 22nd Eur. Signal Process. Conf. (EUSIPCO)*, 2014, pp. 1392–1396.

[18] K. K. Kamarajugadda and P. Movva, "Periocular region based biometric identification using SIFT and SURF key point descriptors," in *Proc. IEEE 10th Annu. Inf. Technol., Electron. Mobile Commun. Conf. (IEMCON)*, Oct. 2019, pp. 968–972, doi: 10.1109/IEMCON.2019.8936271.

[19] H. Hwang and E. C. Lee, "Near-infrared image-based periocular biometric method using convolutional neural network," *IEEE Access*, vol. 8, pp. 158612–158621, 2020, doi: 10.1109/ACCESS.2020.3020142.

[20] Z. Zhao and A. Kumar, "Improving periocular recognition by explicit attention to critical regions in deep neural network," *IEEE Trans. Inf. Forensics Security*, vol. 13, no. 12, pp. 2937–2952, Dec. 2018, doi: 10.1109/TIFS.2018.2833018.

[21] A. Gangwar and A. Joshi, "Robust periocular biometrics based on local phase quantisation and Gabor transform," in *Proc. 7th Int. Congr. Image Signal Process.*, Oct. 2014, pp. 714–720, doi: 10.1109/CISP.2014.7003871.

[22] F. Caglar and B. Cavusoglu, "Rotation invariant features of wavelet transform for texture retrieval," in *Proc. IEEE Int. Symp. Signal Process. Inf. Technol.*, Dec. 2013, pp. 368–373, doi: 10.1109/ISSPIT.2013.6781909.

[23] F. C. A. Fernandes, R. L. C. V. Spaendonck, and C. S. Burrus, "A new framework for complex wavelet transforms," *IEEE Trans. Signal Process.*, vol. 51, no. 7, pp. 1825–1837, Jul. 2003, doi: 10.1109/TSP.2003.812841.

[24] C. Barajas-García, S. Solorza-Calderón, and E. Gutiérrez-López, "Scale, translation and rotation invariant wavelet local feature descriptor," *Appl. Math. Comput.*, vol. 363, Dec. 2019, Art. no. 124594, doi: 10.1016/J.AMC.2019.124594.

[25] Q. Li, L. Shen, S. Guo, and Z. Lai, "WaveCNet: Wavelet integrated CNNs to suppress aliasing effect for noise-robust image classification," *IEEE Trans. Image Process.*, vol. 30, pp. 7074–7089, 2021, doi: 10.1109/TIP.2021.3101395.

[26] S. M. Anzar and T. Amrutha, "Efficient wavelet based scale invariant feature transform for partial face recognition," in *Proc. AIP Conf.*, 2020, Art. no. 030017, doi: 10.1063/5.0004581.

[27] A. Khmag, "Additive Gaussian noise removal based on generative adversarial network model and semi-soft thresholding approach," *Multimedia Tools Appl.*, 2022, doi: 10.1007/s11042-022-13569-6.

[28] R. R. Coifman and M. V. Wickerhauser, "Entropy-based algorithms for best basis selection," *IEEE Trans. Inf. Theory*, vol. 38, no. 2, pp. 713–718, Mar. 1992, doi: 10.1109/18.119732.

[29] L. Brechet, M.-F. Lucas, C. Doncarli, and D. Farina, "Compression of biomedical signals with mother wavelet optimization and best-basis wavelet packet selection," *IEEE Trans. Biomed. Eng.*, vol. 54, no. 12, pp. 2186–2192, Dec. 2007, doi: 10.1109/TBME.2007.896596.

[30] S. Esakkirajan, T. Veerakumar, N. Malmurugan, and P. Navaneethan, "Image compression using adaptive wavelet packet and multistage vector quantization," in *Proc. IEEE Region 3rd Int. Conf. Ind. Inf. Syst.*, Dec. 2008, pp. 1–4, doi: 10.1109/ICIINFS.2008.4798404.

[31] F. Faradji, R. K. Ward, and G. E. Birch, "A simple approach to find the best wavelet basis in classification problems," in *Proc. 20th Int. Conf. Pattern Recognit.*, Aug. 2010, pp. 641–644, doi: 10.1109/ICPR.2010.162.

[32] F. Faradji, F. Faradji, R. K. Ward, and G. E. Birch, "Using autoregressive models of wavelet bases in the design of mental task-based BCIs," in *Brain-Computer Interface Systems-Recent Progress and Future Prospects*. Croatia: Intech, 2013.

[33] R. R. Coifman, Y. Meyer, S. Quake, and M. V. Wickerhauser, "Signal processing and compression with wavelet packets," in *Wavelets and Their Applications*. Berlin, Germany: Springer, 1994, pp. 363–379, doi: 10.1007/978-94-011-1028-0_18.

[34] D. Wang, D. Miao, and C. Xie, "Best basis-based wavelet packet entropy feature extraction and hierarchical EEG classification for epileptic detection," *Exp. Syst. Appl.*, vol. 38, no. 11, pp. 14314–14320, 2011, doi: 10.1016/j.eswa.2011.05.096.

[35] B.-H. Yang, G.-Z. Yan, R.-G. Yan, and T. Wu, "Adaptive subject-based feature extraction in brain–computer interfaces using wavelet packet best basis decomposition," *Med. Eng. Phys.*, vol. 29, no. 1, pp. 48–53, Jan. 2007.

[36] R. M. Dansereau, W. Kinsner, and V. Cevher, "Wavelet packet best basis search using generalized Rényi entropy," in *Proc. IEEE Can. Conf. Electr. Comput. Eng. Conf. (CCECE)*, vol. 2, May 2002, pp. 1005–1008, doi: 10.1109/CCECE.2002.1013081.

[37] J.-C. Pesquet, H. Krim, D. Leporini, and E. Hamman, "Bayesian approach to best basis selection," in *Proc. IEEE Int. Conf. Acoust., Speech, Signal Process. Conf.*, vol. 5, May 1996, pp. 2634–2637, doi: 10.1109/ICASSP.1996.548005.

[38] A. Osadchiy, A. Kamenev, V. Saharov, and S. Chernyi, "Signal processing algorithm based on discrete wavelet transform," *Designs*, vol. 5, no. 3, pp. 1–13, 2021, doi: 10.3390/designs5030041.

[39] D. L. Fugal, *Conceptual Wavelets in Digital Signal Processing: An In-Depth, Practical Approach for the N On-Mathematician*. San Diego, CA, USA: Space&Signals Techinal, 2009.

[40] N. Thiamchoo and P. Phukpattaranont, "R peak detection algorithm based on continuous wavelet transform and Shannon energy," *ECTI Trans. Comput. Inf. Technol. (ECTI-CIT)*, vol. 10, no. 2, pp. 167–175, Mar. 2017.

[41] P. S. Addison, *The Illustrated Wavelet Transform Handbook: Introductory Theory and Applications in Science, Engineering, Medicine and Finance*. Boca Raton, FL, USA: Taylor & Francis, 2002.

[42] Y. Mallet, D. Coomans, and O. de Vel, "Wavelet packet transforms and best basis algorithms," *Wavelets Chem.*, vol. 22, pp. 151–164, Jan. 2000.

[43] E. D. Übeyli and G. Güler, "Features extracted by eigenvector methods for detecting variability of EEG signals," *Pattern Recognit. Let.*, vol. 28, no. 5, pp. 592–603, Apr. 2007.

[44] L. W. Tu, *Differential Geometry: Connections, Curvature, and Characteristic Classes*. Berlin, Germany: Springer, 2017.

[45] E. Abbena, S. Salamon, and A. Gray, *Modern Differential Geometry of Curves and Surfaces With Mathematica*. Boca Raton, FL, USA: CRC Press, 2017.

[46] H. Zhang, M. Jiang, and Q. Kou, "Color image retrieval algorithm fusing color and principal curvatures information," *IEEE Access*, vol. 8, pp. 184945–184954, 2020, doi: 10.1109/ACCESS.2020.3030056.

[47] S. Ghaffari, P. Soleimani, K. F. Li, and D. W. Capson, "Analysis and comparison of FPGA-based histogram of oriented gradients implementations," *IEEE Access*, vol. 8, pp. 79920–79934, 2020, doi: 10.1109/ACCESS.2020.2989267.

[48] F. M. Algashaam, K. Nguyen, V. Chandran, and J. Banks, "Elliptical higher-order-spectra periocular code," *IEEE Access*, vol. 5, pp. 6978–6988, 2017, doi: 10.1109/ACCESS.2017.2697898.

[49] G. Mahalingam and K. Ricanek, "Is the eye region more reliable than the face? A preliminary study of face-based recognition on a transgender dataset," in *Proc. IEEE 6th Int. Conf. Biometrics, Theory, Appl. Syst. (BTAS)*, Sep. 2013, pp. 1–7, doi: 10.1109/BTAS.2013.6712710.

[50] N. Dalal and B. Triggs, "Histograms of oriented gradients for human detection," in *Proc. IEEE Comput. Soc. Conf. Comput. Vis. Pattern Recognit. (CVPR)*, vol. 1, Jun. 2005, pp. 886–893, doi: 10.1109/CVPR.2005.177.

[51] V. H. Schultheiss, S. Batz, and U. Peschel, "Light in curved two-dimensional space," *Adv. Phys., X*, vol. 5, no. 1, 2020, Art. no. 1759451, doi: 10.1080/23746149.2020.1759451.

[52] M. V. Wickerhauser, *Adapted Wavelet Analysis: From Theory to Software*. Boca Raton, FL, USA: CRC Press, 1996.

[53] C. Thrane, *Doing Statistical Analysis: A Student's Guide to Quantitative Research*. New York, NY, USA: Routledge, 2022.

[54] C. N. Padole and H. Proenca, "Periocular recognition: Analysis of performance degradation factors," in *Proc. 5th IAPR Int. Conf. Biometrics (ICB)*, Mar. 2012, pp. 439–445, doi: 10.1109/ICB.2012.6199790.

[55] A. S. Georghiades, P. N. Belhumeur, and D. Kriegman, "From few to many: Illumination cone models for face recognition under variable lighting and pose," *IEEE Trans. Pattern Anal. Mach. Intell.*, vol. 23, no. 6, pp. 643–660, Jun. 2001, doi: 10.1109/34.927464.

[56] K.-C. Lee, J. Ho, and D. Kriegman, "Acquiring linear subspaces for face recognition under variable lighting," *IEEE Trans. Pattern Anal. Mach. Intell.*, vol. 27, no. 5, pp. 684–698, May 2005, doi: 10.1109/TPAMI.2005.92.

[57] R. Lionnie, C. Apriono, and D. Gunawan, "Face mask recognition with realistic fabric face mask data set: A combination using surface curvature and GLCM," in *Proc. IEEE Int. IoT, Electron. Mechatron. Conf. (IEMTRONICS)*, Apr. 2021, pp. 1–6, doi: 10.1109/IEMTRONICS52119.2021.9422532.

[58] R. M. Haralick, K. Shanmugam, and I. Dinstein, "Textural features for image classification," *IEEE Trans. Syst., Man, Cybern.*, vol. SMC-3, no. 6, pp. 610–621, Nov. 1973, doi: 10.1109/TSMC.1973.4309314.

[59] D. F. Walnut, *An Introduction to Wavelet Analysis*. Boston, MA, USA: Birkhauser, 2013.
[60] P. Kumari and K. R. Seeja, "An optimal feature enriched region of interest (ROI) extraction for periocular biometric system," *Multimedia Tools Appl.*, vol. 80, no. 24, pp. 33573–33591, Oct. 2021, doi: 10.1007/S11042-021-11402-0.
[61] S. Bharadwaj, H. S. Bhatt, M. Vatsa, and R. Singh, "Periocular biometrics: When iris recognition fails," in *Proc. 4th IEEE Int. Conf. Biometrics, Theory, Appl. Syst. (BTAS)*, Sep. 2010, pp. 1–6, doi: 10.1109/BTAS.2010.5634498.
[62] B.-S. Oh, K. Oh, and K.-A. Toh, "On projection-based methods for periocular identity verification," in *Proc. 7th IEEE Conf. Ind. Electron. Appl. (ICIEA)*, Jul. 2012, pp. 871–876, doi: 10.1109/ICIEA.2012.6360847.
[63] I. Daubechies and C. Heil, "Ten lectures on wavelets," *Comput. Phys.*, vol. 6, no. 6, p. 697, 1992, doi: 10.1063/1.4823127.
[64] C. Tensmeyer and T. Martinez, "Analysis of convolutional neural networks for document image classification," in *Proc. 14th IAPR Int. Conf. Document Anal. Recognit. (ICDAR)*, Nov. 2017, pp. 388–393, doi: 10.1109/ICDAR.2017.71.
[65] Y. G. Jung, C. Y. Low, J. Park, and A. B. J. Teoh, "Periocular recognition in the wild with generalized label smoothing regularization," *IEEE Signal Process. Lett.*, vol. 27, pp. 1455–1459, 2020, doi: 10.1109/LSP.2020.3014472.
[66] S. Ramachandra and S. Ramachandran, "Region specific and subimage based neighbour gradient feature extraction for robust periocular recognition," *J. King Saud Univ.-Comput. Inf. Sci.*, 2022. [Online]. Available: https://www.sciencedirect.com/science/article/pii/S1319157822002403, doi: 10.1016/j.jksuci.2022.07.013.
[67] A. F. M. Raffei, T. Sutikno, H. Asmuni, R. Hassan, R. M. Othman, S. Kasim, and M. A. Riyadi, "Fusion iris and periocular recognitions in non-cooperative environment," *Indonesian J. Electr. Eng. Informat. (IJEEI)*, vol. 7, no. 3, pp. 543–554, Oct. 2019, doi: 10.52549/IJEEI.V7I3.1147.
[68] P. Bi, Y. Deng, and X. Du, "A robust optimal mean cosine angle 2DPCA for image feature extraction," *Neural Comput. Appl.*, vol. 2022, pp. 1–18, Jul. 2022, doi: 10.1007/S00521-022-07572-Z.
[69] S. Chakraborty, S. K. Singh, and P. Chakraborty, "Local gradient hexa pattern: A descriptor for face recognition and retrieval," *IEEE Trans. Circuits Syst. Video Technol.*, vol. 28, no. 1, pp. 171–180, Jan. 2018, doi: 10.1109/TCSVT.2016.2603535.
[70] S. Chakraborty, S. K. Singh, and K. Kumar, "Facial biometric system for recognition using extended LGHP algorithm on raspberry Pi," *IEEE Sensors J.*, vol. 20, no. 14, pp. 8117–8127, Jul. 2020, doi: 10.1109/JSEN.2020.2979907.
[71] Q. Shi, P. N. Suganthan, and J. D. Ser, "Jointly optimized ensemble deep random vector functional link network for semi-supervised classification," *Eng. Appl. Artif. Intell.*, vol. 115, Oct. 2022, Art. no. 105214, doi: 10.1016/J.ENGAPPAI.2022.105214.
[72] G. Y. Chen, A. Krzyžak, P. Duda, and A. Cader, "Noise robust illumination invariant face recognition via bivariate wavelet shrinkage in logarithm domain," *J. Artif. Intell. Soft Comput. Res.*, vol. 12, no. 3, pp. 169–180, 2022, doi: 10.2478/jaiscr-2022-0011.
[73] G. Y. Chen, W. Xie, and A. Krzyzak, "Illumination invariant face recognition using directional gradient maps," in *Proc. Int. Conf. Intell. Comput.*, 2022, pp. 330–338, doi: 10.1007/978-3-031-13870-6_27.
[74] Y. Wang, Z. Li, F. Li, P. Yang, and J. Yue, "Towards fusing fuzzy discriminative projection and representation learning for image classification," *Eng. Appl. Artif. Intell.*, vol. 114, Sep. 2022, Art. no. 105137, doi: 10.1016/J.ENGAPPAI.2022.105137.
[75] L. Feng-Yao, H. Chang-Hui, and L. Yu, "QRCP-based preprocessing for illumination invariant measure under severe illumination variations," *Signal, Image Video Process.*, 2022, doi: 10.1007/S11760-022-02283-3.
[76] G.-S.-J. Hsu, H.-Y. Wu, C.-H. Tsai, S. Yanushkevich, and M. L. Gavrilova, "Masked face recognition from synthesis to reality," *IEEE Access*, vol. 10, pp. 37938–37952, 2022, doi: 10.1109/ACCESS.2022.3160828.
[77] W. Hariri, "Efficient masked face recognition method during the COVID-19 pandemic," *Signal, Image Video Process.*, vol. 16, no. 3, pp. 605–612, Apr. 2022, doi: 10.1007/S11760-021-02050-w.
[78] Y. Li, K. Guo, Y. Lu, and L. Liu, "Cropping and attention based approach for masked face recognition," *Appl. Intell.*, vol. 51, no. 5, pp. 3012–3025, 2021, doi: 10.1007/S10489-020-02100-9.
[79] M. Zhang, R. Liu, D. Deguchi, and H. Murase, "Masked face recognition with mask transfer and self-attention under the COVID-19 pandemic," *IEEE Access*, vol. 10, pp. 20527–20538, 2022, doi: 10.1109/ACCESS.2022.3150345.
[80] G. Wu, "Masked face recognition algorithm for a contactless distribution cabinet," *Math. Problems Eng.*, vol. 2021, pp. 1–11, May 2021, doi: 10.1155/2021/5591020.

REGINA LIONNIE (Graduate Student Member, IEEE) received the B.Eng. degree in electronic engineering from Universitas Kristen Satya Wacana, in 2012, and the M.Eng. degree in electrical engineering from Universitas Mercu Buana Jakarta, in 2018. She is currently pursuing the Ph.D. degree with the Department of Electrical Engineering, Universitas Indonesia. Her main research interests include biometrics recognition, pattern recognition, and image processing.

CATUR APRIONO (Member, IEEE) received the B.Eng. and M.Eng. degrees in telecommunication engineering from the Department of Electrical Engineering, Universitas Indonesia, Indonesia, in 2009 and 2011, respectively, and the Ph.D. degree in nano vision technology from Shizuoka University, Japan, in 2015. Since 2018, he has been an Assistant Professor of telecommunication engineering with the Universitas Indonesia, where he is currently a Lecturer with the Department of Electrical Engineering, Faculty of Engineering. His main research interests include antenna and microwave engineering, terahertz wave technology, and optical communications. He has been a member of the IEEE Antenna and Propagation Society (AP-S) and the IEEE Microwave Theory and Technique Society (MTT-S). He had involvement in the IEEE Joint Chapter MTT/AP Indonesia Section as a Secretary and a Treasurer, in 2017, 2018, and 2019, and he was active in various chapter activities, such as the First Indonesia–Japan Workshop on Antennas and Wireless Technology (IJAWT) as a Secretary and the 2019 IEEE International Conference on Antenna Measurements Applications (CAMA), Bali, as a Treasurer, in October 2019.

RIFAI CHAI (Senior Member, IEEE) received the B.Eng. degree from Krida Wacana Christian University, Jakarta, Indonesia, in 2000, and the Ph.D. degree in engineering from the University of Technology Sydney (UTS), in 2014. From 2000 to 2010, he worked at companies in Indonesia and Australia as a Product Development Engineer, a Research and Development Engineer, and a Project Engineer. He worked with the University of Technology Sydney as an Associate Lecturer and a Lecturer, from 2012 to 2018. He is currently working as a Senior Lecturer with the School of Science, Computing and Engineering Technologies, Swinburne University of Technology, Melbourne, VIC, Australia. His research interests include artificial intelligence, autonomous systems, brain–computer interfaces, and medical signal processing and devices. He serves as an Associate Editor for *Electronics Letters*.

DADANG GUNAWAN (Senior Member, IEEE) received the bachelor's degree in electrical engineering from the University of Indonesia, in 1983, the master's degree from Keio University, Japan, in 1989, and the Ph.D. degree from the University of Tasmania, Australia, in 1995. He is currently a Professor with the Department of Electrical Engineering, Universitas Indonesia. He has published hundreds of academic papers as a first author or a coauthor in proceedings and international journals. His research interests include wireless and signal processing technology.